

Metasomatism in the Finero Phlogopite Peridotite: New insights from C and N concentrations and $\delta^{13}\text{C}$ - $\delta^{11}\text{B}$ signatures

E. Cannà^{a,*}, M. Tiepolo^a, P. Fumagalli^a, G. Grieco^a, S. Agostini^b

^a Dipartimento di Scienze della Terra "A. Desio", Università di Milano, Via S. Botticelli 23, 20133 Milano, Italy

^b Istituto di Geoscienze e Georisorse, CNR, Via Moruzzi 1, 56124 Pisa, Italy

ARTICLE INFO

Editor: Don Porcelli

Keywords:

Carbon-Nitrogen cycles
Mantle metasomatism
Sub-continental lithospheric mantle
C-B isotopes
Finero Peridotite

ABSTRACT

The interconnection between element recycling and mantle metasomatism may provide powerful insights to unravel the mechanisms governing the transfer, partitioning and residence times of volatiles among the different Earth's reservoirs. In this study, we provide new constraints on the incorporation of C and N in the rock-forming minerals of the Finero Phlogopite Peridotite (FPP) from the Ivrea-Verbano Zone (Southern Alps, Italy), representing a natural laboratory to shed lights on the amounts of volatiles that may be fixed in a deeply metasomatized sub-continental lithospheric mantle (SCLM). Constraints on the relationships between metasomatic events and volatile element enrichment were given by *in-situ* LA-ICP-MS and micro-Raman investigations together with C ($\delta^{13}\text{C}$) and B ($\delta^{11}\text{B}$) isotopes.

All rock-forming minerals (olivine, clinopyroxene, amphibole and phlogopite) show enrichments in C (270–690 ppm) and N (7–20 ppm) compared to depleted mantle values. The high volatile contents in clinopyroxene and in amphibole are associated with enrichment in incompatible elements (e.g., Li, B, Rb, Sr, Pb, Th, U) and high $\text{La}_\text{N}/\text{Lu}_\text{N}$ ratios (up to 42.0) thus confirming that the metasomatic agent affecting the FPP derive from a hydrous melt with crustal affinity enriched in C and N. Micro-Raman investigations document the occurrence of graphite, carbonate and N_2 inclusions, specifically in olivine and clinopyroxene, that are likely responsible for the high C–N concentrations reported here. The $\delta^{13}\text{C}$ signatures measured in mineral separates range from –12.6 to –22.7 ‰, suggesting an overprinting of the C mantle signature by a ^{12}C -rich crustal metasomatic agent. High temperature decarbonation processes, simulated by heating the samples up to 900 °C, indicate that up to 10 ppm of C can be residually stored in the SCLM, whereas N is completely released even at lower temperature. The LA-MC-ICP-MS *in-situ* $\delta^{11}\text{B}$ signature of amphibole is -5.4 ± 4.1 ‰ (2σ , $n = 18$), whereas bulk $\delta^{11}\text{B}$ of olivine and clinopyroxene is -5.51 ± 0.01 ‰ (2σ) and -1.82 ± 0.06 ‰ (2σ), respectively. Modelling shows that residual slab melts plus variable amounts of ^{11}B -rich serpentinite-derived fluids may account for these B isotope imprints. A subduction-related metasomatizing event during the FPP's evolution is thus proposed to explain the geochemical features documented in our study, in agreement with previous works. At global scale, our results suggest that the metasomatized SCLM might significantly contribute to the so-called hidden C reservoir invoked to match the global C mass balance calculations.

1. Introduction

The processes and the scales of volatiles recycle within the Earth's system are complex, poorly understood and still under evaluation (Barry et al., 2019; Barry and Hilton, 2016; Bebout, 2014; Busigny et al., 2019; Cannà et al., 2020; Dasgupta and Grewal, 2019; Galloway et al., 2004; Gonzalez et al., 2016; Halama et al., 2014, 2021; Hutchison et al., 2019; Kendrick et al., 2017; Marty et al., 2020; Plank and Manning, 2019; Schwarzenbach et al., 2018; Vitale Brovarone et al., 2017). Among

geodynamic environments, subduction zones are the most relevant sites where the injection of incompatible- and volatile-rich materials are processed and modified through their journey to depths, driving the elements recycle (Cannà and Malaspina, 2018, and references therein) at least since the onset of modern plate tectonics. Because volatiles are the building blocks of the molecules at the base of life as we know, particular interest has been devoted to the understanding of the mechanisms governing the volatiles exchanges, partitioning and residence times in the different Earth's reservoirs (Cartigny and Marty, 2013;

* Corresponding author.

E-mail address: enrico.canna@unimi.it (E. Cannà).

<https://doi.org/10.1016/j.chemgeo.2022.121181>

Received 17 July 2022; Received in revised form 10 October 2022; Accepted 15 October 2022

Available online 21 October 2022

0009-2541/© 2022 Elsevier B.V. All rights reserved.

Dasgupta and Grewal, 2019; Mallik et al., 2018). All together, this information is essential to unravel the impact of subduction processes on the volatiles cycle and to correctly estimate their fluxes at planetary scale (Plank and Manning, 2019; Zerkle and Mikhail, 2017).

An increasing number of works highlights that significant amounts of volatiles (e.g., C, N, Cl, F and H₂O) and incompatible and fluid-mobile elements (e.g., Cs, Ba, FME: B, Li, As, Sb, Pb, Sr) are removed earlier during subduction down to 200 km depth, depending on the thermal regime of the subduction setting (Van Keken et al., 2002). The fate of these volatiles – referred here to as C-N-bearing aqueous fluids/hydrous melts – is to infiltrate upward in the supra-subduction mantle wedge, inducing its metasomatism and/or triggering its partial melting leading to the development of arc magmatism. In the latter case, a significant amount of volatiles can return to the atmosphere via outgassing during volcanic activity (Wallace et al., 2015) ensuring a relatively short timespan of recycle (from ka to Ma; Baldwin et al., 2021). By contrast, during mantle metasomatism new minerals can form (e.g., clinopyroxenes, amphiboles, micas, carbonates; Ionov et al., 1997; Ionov and Hofmann, 1995; Sapienza et al., 2009), ensuring volatiles storage on long geological timescales (from hundreds of Ma to up to Ga; Kelemen and Manning, 2015). Associated to the mobilization of volatiles, also FMEs are transported via fluids and melts from the downgoing slab to the overlying mantle thus generating FME-enriched arc volcanic rocks (Porter and White, 2009). Among FMEs used to investigate chemical evolution in slab-derived (i.e., high-pressure) rocks, arc volcanic products and mantle xenoliths, boron (B) and its isotopes are particular sensitive geochemical tracers, able to unravel subduction processes. Because slab reservoirs (i.e., sediments, altered oceanic crust and lithospheric mantle) have B isotopic signatures (De Hoog and Savov, 2018) distinct from those of uncontaminated Earth's mantle (Marschall et al., 2017), B isotopes (expressed as $\delta^{11}\text{B}$) can be used to disclose metasomatic sources in mantle domains (e.g., Tomanikova et al., 2019). In this context, the Finero Phlogopite Peridotite (FPP) from the Ivrea-Verbano Zone (IVZ) outcropping in the Southern Alps (Italy) represents a natural laboratory to unravel the amounts of volatiles stored in metasomatized mantle domains (e.g., Zanetti et al., 1999). In this terrane, a complete tilted section of deep continental crust and mantle rocks are exposed (Fountain, 1976; Wolff et al., 2012). According to literature, the FPP (together with other mantle bodies within the IVZ) represents a very well characterized portion of metasomatized subcontinental lithospheric mantle (SCLM) (Proureau et al., 2001). The behaviour and budget of trace elements of the FPP in pre- and syn-metasomatic minerals are well documented (Corvò et al., 2020; Zanetti et al., 1999) together with the whole-rock isotopic composition of several isotopic systematics (i.e., Sr, Pb, Nd) (Cumming et al., 1987; Hartmann and Wedepohl, 1993; Lu et al., 1997), however, its C and N budgets (Ferraris et al., 2004) and B isotope composition are still poorly known. It is widely accepted that crustal-derived metasomatism of the FPP plays an important role in the chemical refertilization of the SCLM. However, there is an ongoing debate aimed to correctly understand whether the metasomatism occurred as a single event or it reflects multiple inputs of crustal materials, referred to as a precursor hydrous C-bearing melt followed by C-rich aqueous fluids (Grieco et al., 2001; Zaccarini et al., 2004). Concurrently, the geodynamic evolution of the FPP is still controversial and the setting responsible for the metasomatic imprint is still under evaluation – i.e., subduction-related vs. extensional tectonics (Bussolesi et al., 2019; Zaccarini et al., 2004; Zanetti et al., 1999).

Here, we present a detailed study on the total C and N concentrations and total C isotope composition ($\delta^{13}\text{C}$) on mineral separates of the FPP. Particular interest has been devoted to characterizing the volatile species entrapped as primary and pseudo-secondary inclusions within recrystallized olivine and metasomatized minerals by using micro-Raman technique. We provide *in-situ* laser ablation (LA-) ICP-MS trace element data on rock-forming minerals and both *in-situ* B isotope composition of metasomatic amphibole and bulk B isotope composition

of olivine and clinopyroxene separates. These data are discussed in order to shed new light on the source of the metasomatism affecting the FPP and more in general the fate of C–N during melt migration in the SCLM.

2. Geological background

The Ivrea-Verbano Zone (IVZ, Italy) is a NE-SW elongated body of continental crust section belonging to the Southern Alpine basement (Fig. 1). It is interpreted as a remnant of the continental margin of the Adriatic micro-plate dismembered during the opening of the Ligurian-Piedmont oceanic basin and escaped Alpine subduction (Schmid, 1993). The IVZ mainly consists of slivers of intermediate to deep continental crust and mantle rocks now exposed due to tilting of about 90° and uplift after the Alpine collision. It outcrops between the Insubric, the Cossato-Mergozzo-Brissago (CMB) and the Cremona Lines (Fountain, 1976; Handy et al., 1999; Rutter et al., 2007; Wolff et al., 2012) (Fig. 1A). The metamorphic conditions increase towards the contact with the Insubric Line suggesting that progressively shallower crustal levels are exposed on the eastern side of the IVZ.

From the top to the bottom the IVZ can be subdivided in three major units: the Kinzigite Formation, the Mafic Complex and the Mantle Peridotites (Fig. 1A). The Kinzigite Formation outcrops close to the CMB Line and is made by sequences of sedimentary and volcanic rocks metamorphosed showing amphibolite- to granulite-facies re-equilibration. The Mafic Complex consists of gabbroic bodies intruded within the Kinzigite Formation at 295–280 Ma (Peressini et al., 2007). The Mantle Peridotite unit comprise different mantle masses among which the Balmuccia and Finero are the major bodies (Mazzucchelli et al., 1992) (Fig. 1A).

The Finero mafic-ultramafic complex is located in the northernmost part of the IVZ in contact with the Insubric Line (Fig. 1A) and is composed by the Finero Phlogopite Peridotite (FPP) unit which is in contact with the Finero mafic complex (Fig. 1B). The latter consists of an intercalation of mafic-ultramafic lithologies (External Gabbro, Amphibole Peridotite and Layered Internal Zone) interpreted as pristine intrusive bodies (Coltorti, 1984). The FPP is representative of metasomatized lithospheric mantle materials and consists of phlogopite-bearing harzburgites associated with phlogopite-bearing pyroxenites (Mazzucchelli et al., 2014). These rocks mainly show a complete recrystallization in response to pervasive to channelized melt migration forming dunitic bodies mainly elongated parallel to the mantle foliation and often incorporating stratiform to podiform chromitites and, less frequently, layers made of pyroxenite and hornblendites (Grieco et al., 2001, 2004; Zanetti et al., 2016).

According to petrographic and geochemical features, the metasomatism in the FPP is indicative of a multistage evolution. The extraction of about 18% of basaltic MORB melt, which results in a peridotite depleted in incompatible elements, predates any metasomatic event (Hartmann and Hans Wedepohl, 1993). Volatile-rich melt percolation(s) leads to pervasive crystallization of large amounts of pargasitic amphibole and phlogopite (Coltorti, 1984) occurring at maximum pressure and temperature (*P-T*) conditions below 2.0 GPa and 980–1080 °C, respectively (Tommasi et al., 2017). Together with these hydrous phases, the metasomatic event(s) also produced apatite and carbonate-bearing domains (Morishita et al., 2003, 2008; Zanetti et al., 1999). During the metasomatic process(es) the FPP body was heterogeneously enriched in incompatible elements that partially to completely overprint the original mantle signatures. Based on literature data (Cumming et al., 1987; Grieco et al., 2001; Hartmann and Hans Wedepohl, 1993; Raffone et al., 2006; Zanetti et al., 1999, 2016), the hydrous melt metasomatic agent(s) had a subduction-like affinity. If metasomatism occurs as multiple inputs of crustal materials, several authors have proposed that hydrous C-bearing melt metasomatism predates interaction with C-rich aqueous fluids (Grieco et al., 2001; Zaccarini et al., 2004).

High resolution TEM of phlogopite crystals from the FPP reveals

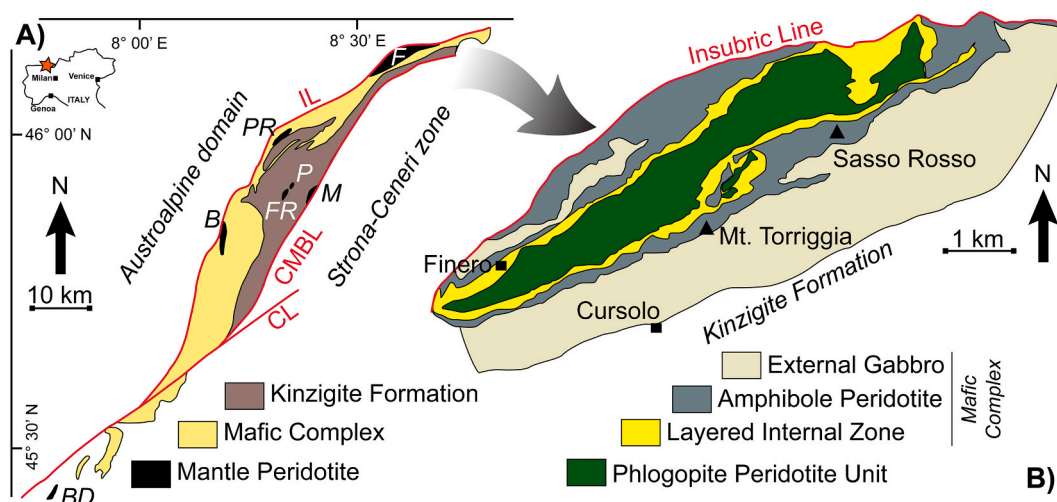


Fig. 1. (A) Schematic map of the Ivrea-Verbano Zone. Major mantle peridotitic bodies are reported (F: Finero, PR: Premosello, P: Alpe Piumero, M: Alpe Morello, FR: Alpe Francesca, B: Balmuccia, BD: Baldissero). IL: Insubric Line; CL: Cremona Line; CMBL: Cossato-Mergozzo-Brissago Line (modified after Quick et al., 1995). (B) Geological map of the Finero Complex (modified after Zanetti et al., 1999).

nanometric intergrowths of graphite-like layers suggesting simultaneous crystallization of both phases from a trapped C-rich hydrous melt. According to literature (Ferraris et al., 2004), the $\delta^{13}\text{C}$ signature of such C points to a mantle-derived origin.

In agreement with the geodynamic model proposed by Zanetti et al. (2016) and based on zircon-bearing chromitite layers within the FPP, the metasomatic history of the FPP starts at mantle depths in the Early Permian (≈ 290 Ma) until its final exhumation and emplacement at crustal levels during Early Jurassic (≈ 180 Ma). The latter event seems to be linked to initiation of continental rifting and mantle exhumation in relation to the opening of the Alpine Tethys. A re-heating to a maximum T of ca. 850°C , followed by rapid cooling is documented by olivine-spinel re-equilibration (Bussolesi et al., 2019). Although the pervasive metasomatism of the FPP occurs at ≈ 290 Ma, an older, Variscan orogenic related age cannot be completely excluded (Zanetti et al., 2016).

3. Sample description

The investigated samples are two phlogopite-bearing harzburgites, samples FFR and FAD1 collected within the olivine mine near the Finero village (WGS84 GPS coordinate: $46^\circ 6' 31''\text{N}$, $8^\circ 33' 8''\text{E}$). Sample FAD1 includes a ~ 5 -cm thick clinopyroxenite vein/dike (hereafter sample FAD2) likely representing the preferential channel for melt migration within the peridotitic body.

Harzburgitic rocks are dominated by olivine with minor modal amounts of ortho- and clino-pyroxenes. They show a granoblastic texture where coarse olivine grains form a mosaic of crystals often with 120° triple junctions. Kink bands in olivine are evidence for metamorphic deformation absent in the other phases. Pyroxenes show medium grain sizes and are randomly displaced in the rock, with no preferred orientation with respect to olivine. Amphibole and phlogopite are minor phases and often associated to each other (Fig. 2A, B). They crystallized along olivine grain boundaries and form aggregates displaced within the peridotites with no preferred orientation. Locally, flakes of phlogopite appear displaced along major linear orientation giving to the rock a layering-like texture. Chromite is often associated with amphibole and phlogopite aggregates (Fig. 2A, B) but can also crystallize as single crystals either along silicates grain boundaries or be present as inclusion within coarse grains of olivine (Fig. 2C).

Clinopyroxene in sample FAD2 is coarse in size and shows granoblastic texture with 120° triple junctions suggesting chemical equilibrium (Fig. 2D). Some clinopyroxene grains show exsolution lamellae evidence for partial recrystallization. Locally, small grains of orthopyroxene or

amphibole are surrounded by clinopyroxene crystals (Fig. 2D).

A major feature of all the investigated samples is the occurrence of primary and/or pseudo-secondary trails of inclusions of both solid and fluid/gaseous infilling (Figs. 2E–G, 5) in almost all rock-forming minerals. Noticeably, solid inclusions only characterize olivine and clinopyroxene.

Based on petrographic investigations, neither apatite nor carbonates are present in the mineral assemblage of both harzburgite and clinopyroxenite samples.

4. Methods

4.1. Sample treatment

In order to avoid C contamination, the entire sample preparation process was carried out using C-free materials. Analyses of C and N were conducted on mineral separates. Unaltered sample's chips were crushed, and mineral separates were obtained after sieving and ultrasonically cleaning samples. Each samples' fraction was washed several times with ultrapure water in ultrasonic bath and then cleaned with Suprapur® hydrochloric acid (HCl 6 N) in ultrasonic bath in order to remove potential surficial contamination from inorganic C (i.e., carbonates). A second ultrasonic bath with ultrapure water was carried out in order to completely remove any trace of HCl. Each fraction of samples was checked under the binocular microscope and only clean minerals were chosen. Olivine, clinopyroxene, amphibole and phlogopite separates were then hand-picked for the geochemical analyses. About 300 mg of mineral separates were manually crushed and milled with an agate mortar and used for bulk C, N and $\delta^{13}\text{C}_{\text{TC}}$ determinations (TC: total C). Depending on the amount of available mineral separates, two steps of heating were carried out in order to estimate the amount of reduced C and carbonates potentially hosted in the minerals. About 1.0 to 1.5 g of mineral powder were placed in ceramic crucible and then heated overnight at 550°C . About 300 mg of these materials were used to determine the reduced-free C content of the minerals ($[\text{C}]_{550}$) while the remaining powder were heated a second time at 900°C to eliminate potential C contamination due to carbonates (e.g., Dean, 1974). Similarly, about 300 mg of sample were used to determine the reduced- and carbonate-free content of the minerals ($[\text{C}]_{900}$).

Several olivine and clinopyroxene crystals from sample FAD1 and FAD2, respectively, were manually polished as low as possible with alumina powder (5 and $1\ \mu\text{m}$) to perform micro-Raman spectra of the inclusions.

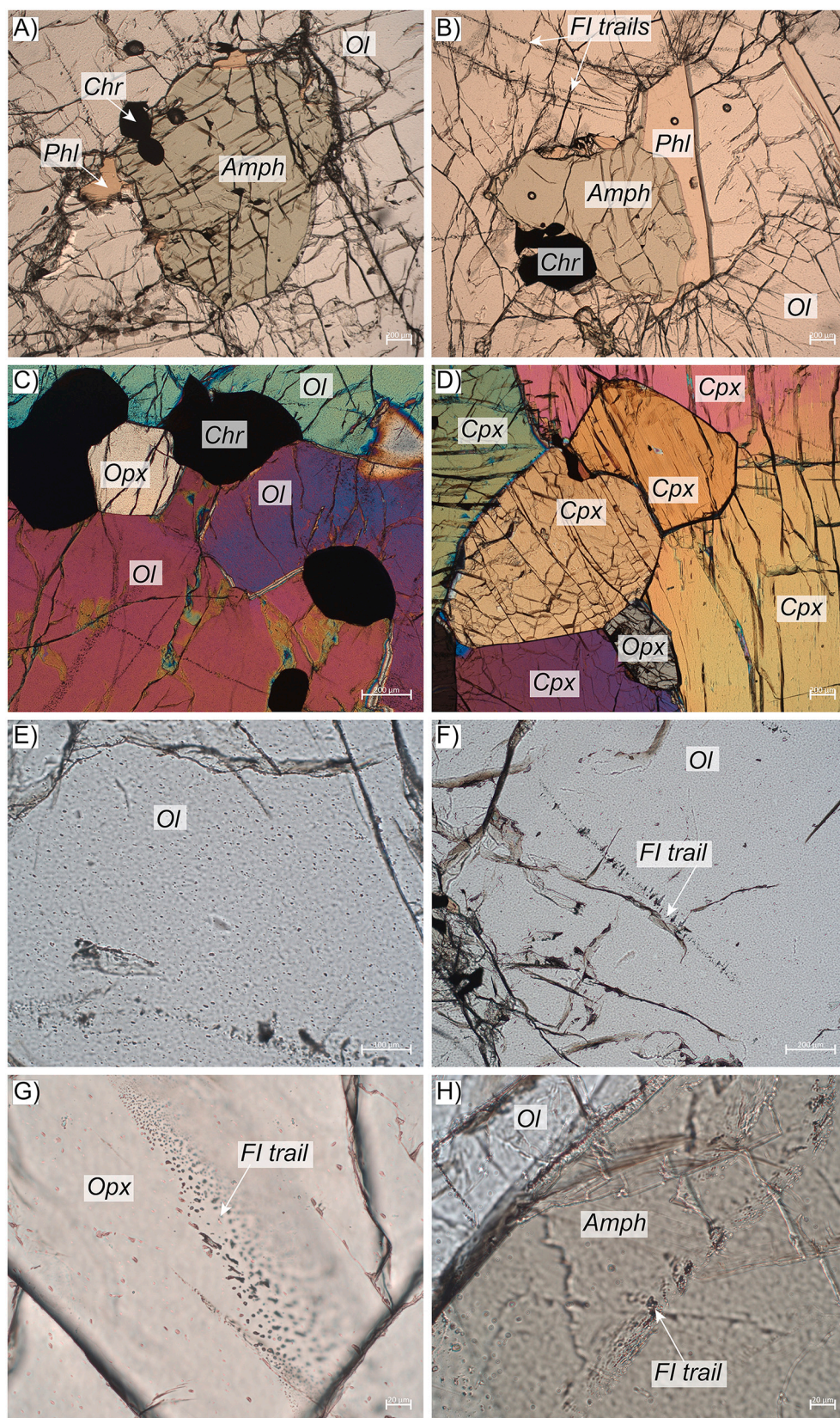


Fig. 2. Petrographic and microstructural features of the investigated samples. Coexistence of amphibole (Amph) and phlogopite (Phl) with chromite (Chr) in sample FAD1 (A) and FFR (B) crystallized along olivine (Ol) grain boundaries. Pseudo-secondary trail of fluid inclusions are also indicated (FI trails; white arrows). (C) Occurrence of chromite in harzburgite from sample FFR. (D) Typical texture in clinopyroxenite from sample FAD2 showing 120° triple junctions suggesting chemical equilibrium. Small grain (s) of orthopyroxene (opx) is also present. (E) Common surface of olivine in sample FFR showing small inclusions. Pseudo-secondary fluid inclusions trails in olivine (sample FFR), orthopyroxene (sample FAD1) and amphibole (sample FAD1) are shown in (F), (G) and (H), respectively.

4.2. Analytical instruments

Trace element mineral composition was determined at the Geochemistry, Geochronology and Isotope Geology Laboratory of the Earth Science Department “A. Desio”, University of Milano LA STATALE (Italy) by laser ablation inductively coupled plasma mass spectrometry (LA-ICP-MS). The instrument couples 193 nm ArF excimer laser ablation microprobe equipped with HelEx II volume sample chamber (Analyte Excite from Teledyne Cetac Technologies) with a single-collector quadrupole ICP-MS (iCAP RQ from Thermo Fisher Scientific). Laser spot size was chosen as large as possible for the analyzed minerals (up to 65 μm) in order to ensure the lowest limits of detection and was carefully positioned to avoid inclusions. The absence of contributions in the ablated material from inclusions was further checked by inspecting the time-resolved spectra for chemical anomalies. The NIST SRM 612 was used as external standard, whereas ^{43}Ca and ^{29}Si were selected as internal standards, depending on the analyzed mineral (see Supplementary Table A1). Quality control was achieved analyzing as unknown in each analytical run the USGS reference basalt glasses GSD-2G and BCR-2G. Precision is better than 10% and accuracy is within 2σ of the preferred values (Supplementary Table A2). A laser fluence of 2.0 J/cm^2 was used for olivine and phlogopite and of 2.5 J/cm^2 for amphibole and clinopyroxene. The laser repetition rate was set to 10 Hz for all minerals. The He flow rate was set to 0.500 l/min and to 0.200 l/min into the sample chamber and in the HelEx II cup, respectively. Each spot was analyzed for a total of 120 s that included 40s of background analyses (comprising 10s of laser warm up), about 60s of laser ablation measuring isotope peak intensity followed by 20s of wash out time. Data reduction was carried out using the Glitter software package (Griffin et al., 2008).

The *in-situ* B isotope composition of the amphibole was measured by LA-MC-ICP-MS technique at the Geochemistry, Geochronology and Isotope Geology Laboratory at the Earth Science Department “A. Desio”, University of Milano LA STATALE (Italy) by coupling the laser system used for the trace element determination to a Neptune XT MC-ICP-MS (Thermo Fisher Scientific). All measurements (*i.e.*, standards and samples) were performed at a repetition rate of 10 Hz, fluence of 3.0 J/cm^2 and in single spot mode with a diameter of 150 μm . Helium flux in the sample chamber and the cup were set to 0.510 l/min and to 0.240 l/min, respectively, to maximize the signal without compromising its stability. Boron isotopes were simultaneously collected on two Faraday cups (^{10}B on L2 and ^{11}B on H4) both connected to $10^{13}\ \Omega$ resistors capable of the highest signal/noise ratios. The instrument is equipped with 0.8 X-skimmer (Ni) + 1.2 Jet sample (Ni) cones and a large dry interface pump (Jet pump). Both $10^{13}\ \Omega$ resistors and mounted cones ensures the maximum sensitivity for isotopic determinations for minerals with low B contents (Lin et al., 2014; Lloyd et al., 2018). Each analyses consisted of 78 cycles of $\sim 1\text{ s}$ each subdivided in 30 cycles of background acquisition, 40 cycles of signal acquisition and 8 cycles of washing time. The addition of $\sim 25\text{ s}$ between each analyses ensures the complete wash out of the gas line. Data reduction was carried out offline with an *in-house* spreadsheet; $^{11}\text{B}/^{10}\text{B}$ ratios exceeding 2σ have been discharged. No downhole isotope ratio fractionation was observed. The results are reported in the common delta(δ)-notation as permil (‰) and expressed relative to the isotopic ratio of the NIST SRM 951 boric acid ($^{11}\text{B}/^{10}\text{B} = 4.04362 \pm 0.00137\ 2\sigma$; (Catanzaro et al., 1970). Instrumental and laser-induced isotope fractionation were evaluated adopting the standard-sample bracketing protocol and using both the NIST SRM612 and the USGS BHVO-2g basaltic glass ($[\text{B}] \sim 34$ and $\sim 5\text{ ppm}$, respectively) as calibrating standard. These reference glasses have $\delta^{11}\text{B}$ of $-0.51 \pm 0.52\text{ ‰}$ (GeoRem mean value) and $-1.82 \pm 0.96\text{ ‰}$ (He et al., 2020), respectively. Recently, the presence of scattered Ca interference on mass 10 was documented to lead to inaccurate $\delta^{11}\text{B}$ results if the B/Ca ratios between the reference standard and the unknowns are unmatched (see Evans et al., 2021 for further details). Remarkably, the similar B/Ca ratio of the BHVO-2g and amphibole is expected to yield accurate B isotope data in amphiboles. Constrain of the accuracy of the measured B isotope

composition for the Finero amphibole has been monitored analyzing an *in-house* reference amphibole (PRG from the Pargas locality, SW Finland) analyzed here with solution-based technique (see below). Hereafter, errors of each single spot analyses is expressed as 2 standard error (2SE), otherwise errors are 2 standard deviation of the mean (2σ).

The B isotope composition of the PRG amphibole used as reference for *in-situ* analyses on amphibole and of olivine and clinopyroxene mineral separates from samples FAD1 and FAD2, respectively, was determined at the IGG-CNR, Pisa (Italy) via Multi-Collector ICP-MS after B extraction from matrix as described in Agostini et al. (2021). Bulk $\delta^{11}\text{B}$ results are relative to the NIST SRM 951 standard (Catanzaro et al., 1970). The purified solutions were measured on a Thermo Fisher Scientific Neptune Plus MC-ICP-MS specially tuned for B isotope analyses and maximum $^{11}\text{B}/^{10}\text{B}$ stability rather than maximum intensity (Foster, 2008). Samples were diluted to contain $\sim 20\text{ ppb}$ of B and were then bracketed with NIST SRM 951 boric acid standard solution of the same concentration, to correct for machine induced mass fractionation. Within run errors are between 0.08 and 0.22‰ (2σ). Several samples were re-repeated and re-analyzed, reproducing the original value to within $\pm 0.5\%$ or better. A detailed description of analytical procedure, along with accuracy of several analyses of NIST SRM 951 and other international and in-house standards is available in Agostini et al. (2021).

Mineral separates were analyzed for their total C content (TC), N concentrations, and C isotope signature ($\delta^{13}\text{C}_{\text{TC}}$) using a Thermo Fischer Organic Elemental Analyzer (OEA, Flash2000) coupled to a Thermo Fischer Delta V Advantage mass spectrometer via a ConFlo IV interface hosted at the IRMS-stable isotope laboratory at the Earth Science Department, University of Milano LA STATALE (Italy). Carbon and N concentrations were calibrated using differing amounts of aspartic acid ($\text{C} = 36.09 \pm 0.27\text{ wt\%}$ and $\text{N} = 10.52 \pm 0.17\text{ wt\%}$); several in-house standards and the international high organic sediment standard ($\delta^{13}\text{C}_{\text{TC}} = -28.85 \pm 0.10\text{‰}$ 2σ ; Elemental Microanalyses Ltd., Certificate No. 295716) were employed for the determination of the C isotope composition. For C we also report the C concentration after heating the samples overnight at 550 and 900 $^{\circ}\text{C}$ ($[\text{C}]_{550}$ and $[\text{C}]_{900}$, respectively). These results are considered as representative of the C content in the samples after the removing of the reduced and inorganic C, respectively. Total C and N concentrations data reported here are the average of 3 replicates (uncertainty of the concentration data $<10\%$), whereas all isotopic analyses for TC are averages of 2 replicates with reproducibility of $\pm 0.2\text{‰}$ (2σ), reported in the standard δ -(delta) notation and expressed relative to VPDB.

A recent analytical investigation (Boocock et al., 2020) pointed out that the Elemental Analyzer fails to fully liberate N from silicate rocks and minerals ensuring a mean N yield of only $44 \pm 10\%$. For this reason, together with unknown and common organic and solid standards, we also analyzed the N content of two reference standards, the UB-N serpentinite and the MA-N granite. These reference materials have 27.5 ± 1.6 and $128.2 \pm 10.3\text{ ppm}$ of N, respectively (Boocock et al., 2020). Our results return an average N concentration of $14.1 \pm 4.5\text{ ppm}$ for the UB-N serpentinite and $50.3 \pm 4.0\text{ ppm}$ for the MA-N granite, pointing to a mean N yield of $45 \pm 9\%$ (Supplementary Table A3), in agreement with the investigation of Boocock et al. (2020). According to this result, the reported N data are corrected by a factor of 2.3 with an estimated relative error of 10% (Table 4) and should be considered as minimum values.

Micro-Raman spectra of solid inclusions hosted within olivine and clinopyroxene were obtained using a Horiba LabRAM HR Evolution hosted at the Earth Science Department, University of Milan (Italy). The instrument was equipped with a green solid-state laser (532 nm) focused through a $100\times$ objective, allowing a spatial resolution of about 1 μm . The signal was dispersed using a 600 g/mm grating and analyzed by a CCD detector. Three to six acquisitions of 60 s were performed for each analyses with a nominal power of 3.2% (*ca.* 1.5 mW) in order to avoid structural perturbation of the graphitic material. The calibration of the spectrometer was checked with a silicon wafer at 520.7 cm^{-1} .

5. Results

5.1. Trace element concentrations

Rare Earth Element (REE) concentrations of clinopyroxenes from harzburgites normalized to CI chondrite (McDonough and Sun, 1995) show enrichment in light (L)-REE over heavy (H)-REE (La_N/Lu_N from 24.2 to 39.0 for sample FAD1 and of 16.4 ± 1.4 for sample FFR) with the latter approaching the chondritic values (Fig. 3A). The LREE of the sample FAD1 are slightly enriched compared to those of the sample FFR. Overall, the REE patterns of the analyzed clinopyroxenes are comparable with those from the apatite-free harzburgite of the FPP available from the literature (e.g., Zanetti et al., 1999; Raffone et al., 2006; Corvò et al., 2020) and with the subhedral grains within harzburgite described by Grieco et al. (2001). The primitive mantle (PM) normalization (McDonough and Sun, 1995) of the incompatible elements shows enrichments in B, Be, Pb, As, Sb (only in one analyses), Sr and Li (Fig. 3B). Thorium and U are enriched only in clinopyroxenes from sample FAD1 while they approach the PM composition in sample FFR. Tungsten is almost one order of magnitude lower than the PM value.

The CI-normalized REE patterns of amphiboles from FAD1 and FFR harzburgites are characterized by a marked enrichment in LREE (100 times CI) over HREE (10 times CI; La_N/Lu_N ratio up to 42 for FAD1 and up to 17 for FFR) and no significant Eu anomaly is observed (Fig. 3C). Amphiboles from sample FAD1 are more LREE enriched with respect to those from sample FFR with La_N/Sm_N ratios of 3.4 and 2.0, respectively. The amphibole crystals displaced in the clinopyroxenite veins (sample FAD2) resemble the REE pattern of the amphiboles in the FAD1 sample (Fig. 3C). Noticeably, amphibole compositions parallel that reported in previous works for apatite-free peridotites (Corvò et al., 2020; Zanetti et al., 1999). Amphiboles have Be, B, Pb, Th and U concentrations 10 to 100 times higher than PM values (McDonough and Sun, 1995) (Fig. 3D). The Nb/Ta and Th/U ratios are above unity in amphibole of both samples (up to 15.6 and 7.8, respectively). When above detection limits, As and Sb are about 10–20 and 5 times the primitive mantle values, respectively and W is enriched with respect to PM value showing positive and negative anomalies compared to neighbour elements for FAD1-FAD2 and FFR samples, respectively. Lithium concentrations are variably depleted trending towards the PM value. Overall, the concentrations of the incompatible element (Ba, Th, U, B, W, Be, Pb, As, Sb and Sr) in amphibole from sample FAD1-FAD2 are higher than those for sample FFR (Fig. 3D).

Olivine has very low or barely detectable REE contents (see Table 1) and, generally, is characterized by high concentrations in transition metals (e.g., Co and Ni up to 142 and 3000 ppm, respectively) and very low concentrations of most of incompatible elements (e.g., Ba, U, Th, Pb, Zr). Lithium ranges from 3.03 to 4.78 ppm and B from 2.36 to 3.47 ppm. Some analyses yield concentrations of As and Sb up to 2–8 times the PM values (McDonough and Sun, 1995) (Fig. 3E). Literature data for the incompatible elements in olivine are scarce and reported only in the recent paper of Corvò et al. (2020), which provides concentrations between 2.1 and 9.1 ppm of Li and from 8.1 to 43 ppm of B in olivine from both deformed and undeformed ultramafic domains.

Phlogopite is characterized by REE concentrations below the detection limits (see Table 1) and shows enrichments in incompatible elements such as Cs, Rb, Ba, B, Pb and Sr normalized to PM (McDonough and Sun, 1995) (Fig. 3F). Arsenic is always below the detection limit (<0.340 ppm), whereas Li, Sb and W are close to PM values. Overall, the incompatible element pattern closely resembles those of phlogopite analyzed so far in other harzburgite/lherzolite samples from the FPP (Corvò et al., 2020; Zanetti et al., 1999).

Clinopyroxenes from the pyroxenite vein (sample FAD2) crosscutting the harzburgite (sample FAD1) are characterized by strong enrichment in LREE compared to HREE (Fig. 3G; La_N/Lu_N ratio from 25.3 to 33.3) and show a La_N/Sm_N ratio up to 2.6 with LREE reaching 30 times the chondritic values (McDonough and Sun, 1995). Overall, also for these

clinopyroxenes their REE pattern resemble those of the clinopyroxene in the apatite-free pyroxenites reported so far in the literature (Corvò et al., 2020; Raffone et al., 2006; Zanetti et al., 1999). Normalized to primitive mantle (McDonough and Sun, 1995), clinopyroxenes are enriched in incompatible elements (Th, U, B, Be, Pb, As, Sb and Sr) with Th/U ratio up to 2.4 (Fig. 3H). Tungsten concentration is almost one order of magnitude lower than the PM value. Compared with published trace element concentrations (Corvò et al., 2020; Raffone et al., 2006; Zanetti et al., 1999), our data resemble those of the apatite-free clinopyroxene from pyroxenites and olivine-bearing websterite although, in the latter, B is significantly higher (up to 25 ppm against 2.3 ppm reported in this work).

5.2. Bulk $\delta^{11}\text{B}$ in olivine and clinopyroxene and in-situ $\delta^{11}\text{B}$ in amphibole

The bulk $\delta^{11}\text{B}$ obtained for the olivine separate in sample FAD1 is $-5.51 \pm 0.01\text{‰}$, whereas the $\delta^{11}\text{B}$ signature of the clinopyroxene separate from sample FAD2 is $-1.31 \pm 0.28\text{‰}$ (Table 2, Fig. 5).

The *in-situ* $\delta^{11}\text{B}$ of the BHVO-2g basaltic glass and of the PRG paragonite obtained using the NIST SRM 612 as calibrating standard are $-11.7 \pm 2.9\text{‰}$ ($n = 12$) and $-25.4 \pm 2.1\text{‰}$ ($n = 12$), significantly lower than their reference solution-based $\delta^{11}\text{B}$ values of $-1.82 \pm 0.96\text{‰}$ (He et al., 2020) and $-16.58 \pm 0.06\text{‰}$ (this study; Table 2, Fig. 4), respectively. In both cases, the mismatch between the reference values and the one obtained with the LA-MC- ICP-MS is ca. -9 to -10‰ (Fig. 4). An accurate $\delta^{11}\text{B}$ value of $-15.9 \pm 1.6\text{‰}$ ($n = 12$) for the PRG reference amphibole was obtained using the BHVO-2g basaltic glass as calibrating standard (Table 2, Fig. 4) given the close matching between their B/Ca ratios. Consequently, all the $\delta^{11}\text{B}$ *in-situ* data reported below for the amphibole were measured using the BHVO-2g as calibrating standard.

The *in-situ* B isotope compositions of the amphibole (Table 3) from the harzburgites are highly variable ranging from $-1.8 \pm 1.6\text{‰}$ (2SE) to $-9.4 \pm 3.1\text{‰}$ (2SE) (Fig. 5) with average values of $-4.9 \pm 3.9\text{‰}$ (2σ , $n = 8$) and $-6.5 \pm 5.6\text{‰}$ (2σ , $n = 4$) for sample FAD1 and FFR, respectively. The $\delta^{11}\text{B}$ signature of the amphibole in the clinopyroxenite vein yields an average value of $-5.3 \pm 3.3\text{‰}$ (2σ , $n = 6$), overlapping that of amphibole in the harzburgites. However, this value is slightly lower than the $\delta^{11}\text{B}$ signature of the coexisting clinopyroxene (Table 2). Overall, the average *in-situ* $\delta^{11}\text{B}$ result for amphiboles of $-5.4 \pm 4.1\text{‰}$ (2σ , $n = 18$, Fig. 5) is comparable with the bulk B isotope compositions reported for the olivine from samples FAD1.

5.3. Carbon and N concentrations and C isotope composition

Carbon concentrations in olivine and phlogopite separates from harzburgites are in the ranges 256–268 ppm and 344–686 ppm, respectively (Table 4). Results on the phlogopite are comparable with those reported by Ferraris et al. (2004). Clinopyroxene from sample FFR shows concentrations of 610 ppm whereas clinopyroxene from sample FAD2 has significantly lower C content (273 ppm; Fig. 6A). Carbon concentration in amphibole is 336 ppm. Mineral separates heated overnight at 550 °C have C concentrations of 48–89 ppm for olivine (corresponding to 82 and 65% of C loss, respectively), 180 ppm for phlogopite (65% of C loss) and 120 ppm for clinopyroxene from sample FAD2 (56% of C loss). Carbon concentrations for samples heated overnight at 900 °C are very low ranging from 5 to 10 ppm (Fig. 6A), reflecting a C loss of >96% compared to not treated samples.

The N contents of the mineral separates range between 14 and 40 ppm (Table 4) and are significantly higher compared to primitive and depleted mantle values (McDonough and Sun, 1995; Salters and Stracke, 2004). The highest value pertains to phlogopite from sample FAD1 while the lower value to the amphiboles of sample FFR. With the exception of olivine from sample FFR, N shows a weak positive correlation with C (Fig. 6B). After heating the samples at 550 and 900 °C, the N concentrations were below detection limits.

Carbon isotope composition ($\delta^{13}\text{C}$) of the untreated mineral

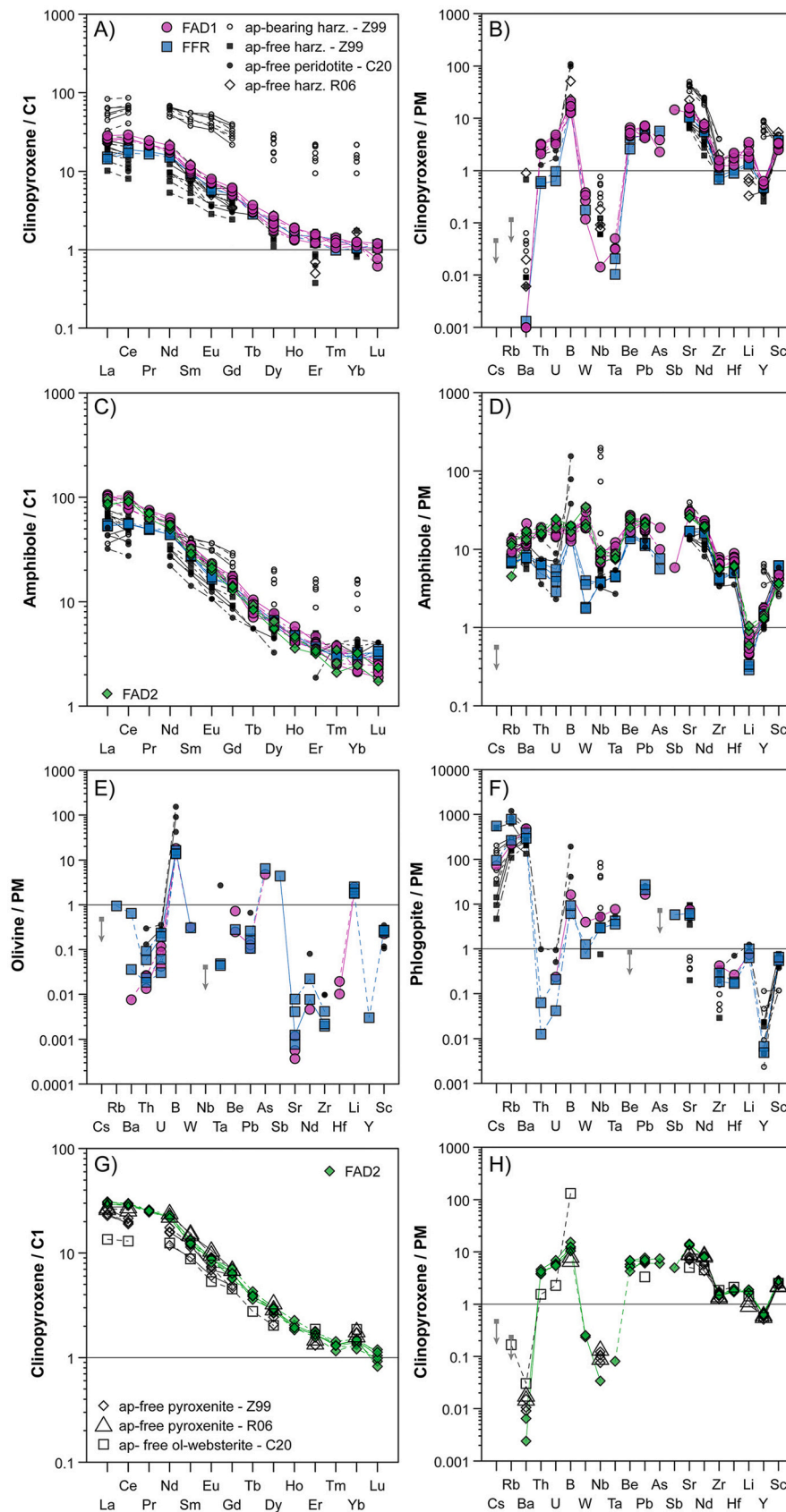


Fig. 3. Chondritic (C1) normalized (McDonough and Sun, 1995) Rare Earth Element (REE) patterns for clinopyroxene and amphibole from sample FFR, FAD1 and FAD2 (A-C-G). Primitive Mantle (PM) normalized incompatible element pattern for clinopyroxene (B–H), amphibole (D), olivine (E) and phlogopite (F). Literature data are from Zanetti et al. (1999; Z99), Raffone et al. (2006; R06) and Corvò et al. (2020; C20).

Table 1

Trace elements concentrations (ppm) of olivine, amphibole, phlogopite and clinopyroxene.

Analyzed isotope	Analyte symbol	FAD1 (harzburgite)								FFR (harzburgite)								FAD2 (clinopyroxenite)							
		Olivine (n = 4)	sd	Clinopyroxene (n = 5)	sd	Amphibole (n = 8)	sd	Phlogopite (n = 2)	sd	Olivine (n = 4)	sd	Clinopyroxene (n = 2)	sd	Amphibole (n = 4)	sd	Phlogopite (n = 2)	sd	Clinopyroxene (n = 6)	sd	Amphibole (n = 3)	sd				
7	Li	3.36	0.38	4.02		1.21	0.843	0.253	1.66	0.66	3.34	0.56	2.15		0.06	0.613	0.221	1.31	0.41	2.78		0.19	1.37	0.37	
9	Be	0.033	0.023	0.370		0.059	1.60	0.23	0.340		0.019		0.230		0.076	1.03	0.09	<0.080		0.385		0.069	1.54	0.23	
11	B	3.07	0.41	2.99		0.67	3.20	0.43	3.06		2.76	0.23	3.08		0.52	2.82	0.19	1.47	0.42	2.29		0.36	3.61	0.38	
45	Sc	4.17	0.25	51.5		6.7	80.3	6.7	9.65	0.01	4.39	0.22	63.4		0.9	102	5	10.3	1.3	47.5		0.7	61.3	3.0	
49	Ti	9.25	2.56	651		105	6914	496	10,413	233	9.23	2.78	459		26	4286	354	7203	1223	834		27	8077	580	
51	V	0.234	0.071	82.6		8.3	291	42	166	4	0.377	0.121	98.7		2.7	325	8	198	6	87.1		3.3	330	42	
53	Cr	11.2	4.0	5102		636	17,607	2987	9696	469	10.3	7.6	3780		249	14,469	219	9740	730	6014		316	20,511	2886	
55	Mn	988	15	565		29	417	87	74.4	6.9	949	31	532		10	322	18	64.9	7.9	630		11	467	31	
59	Co	133	4	17.0		1.9	35.5	5.9	44.1	0.1	142	1	17.0		0.3	30.6	0.6	42.2	3.9	18.9		0.4	40.9	4.1	
60	Ni	2714	73	271		27	812	139	1367	1	3076	50	291		1	749	18	1532	30	314		10	969	85	
65	Cu	0.400	0.108	0.356		0.154	0.608	0.280	0.990	0.354	0.348	0.102	0.164		0.028	0.677	0.316	0.640		0.440		0.096	<4.12		
66	Zn	48.2	1.2	7.07		1.03	15.1	2.4	16.4	2.9	47.0	1.0	6.91		0.23	12.81	0.43	13.7	4.2	8.41		0.40	17.1	1.4	
75	As	0.240		0.153		0.055	0.725	0.318	<0.970		0.320		0.285			0.330	0.071	<0.330		0.335		0.049	<0.990		
85	Rb	<0.162		<0.071			5.61	1.22	310	256	0.569		<0.070			4.18	0.27	316	220	<0.165			5.60	2.51	
88	Sr	0.014	0.008	289		34	572	25	152	1	0.069	0.064	208		1	337	3	118	7	270		8	526	32	
89	Y	<0.009		2.38		0.18	6.63	0.66	0.023		0.013		2.09		0.10	6.29	0.16	0.025	0.005	2.76		0.10	5.81	0.30	
90	Zr	<0.010		13.5		1.9	72.2	5.8	4.80	0.63	0.029	0.012	7.42		0.74	42.9	1.5	2.46	0.75	15.5		0.6	58.3	1.7	
93	Nb	<0.020		0.009			5.21	0.64	3.59	0.21	<0.019		<0.005			2.49	0.04	1.95	0.04	0.022		0.009	5.68	0.91	
111	Cd	<0.219		0.127		0.008	<0.240		<0.870			<0.189	0.120			<0.189		<0.260		0.208		0.081	0.146		
121	Sb	<0.023		0.080			0.032		<0.121			0.024	<0.015			<0.024		0.032		0.027		0.011	<0.064		
133	Cs	<0.010		<0.001			<0.012		6.59	7.19	<0.010		<0.001			<0.013		6.83	6.82	<0.010			<0.014		
137	Ba	0.050		0.004		0.001	92.9	23.2	3291	130	2.25	2.85	0.009			52.1	2.0	2258	439	0.029		0.019	102	13	
139	La	<0.003		6.14		0.36	23.4	1.3	0.016	0.016	0.015	0.012	3.50		0.17	12.7	0.3	0.009	0.002	7.15		0.17	21.0	1.6	
140	Ce	0.004	0.004	16.1		1.0	55.5	6.1	0.021		0.017	0.022	11.0		0.8	34.1	0.4	0.003	0.004	17.9		0.3	57.5	2.3	
141	Pr	<0.002		2.06		0.13	6.36	0.41	<0.013		0.006		1.59		0.09	4.68	0.13	<0.003		2.35		0.04	6.29	0.41	
146	Nd	0.006		8.64		0.64	25.4	2.1	0.010		0.019	0.013	7.08		0.28	20.6	0.7	<0.021		10.2		0.2	23.7	1.2	
149	Sm	<0.020		1.53		0.14	4.63	0.37	<0.119		<0.017		1.39		0.00	4.08	0.06	<0.026		1.88		0.09	4.37	0.36	
151	Eu	0.004		0.413		0.023	1.20	0.06	0.036	0.018	<0.006		0.335		0.023	0.973	0.040	0.029	0.007	0.493		0.019	1.20	0.09	
157	Gd	0.053		1.10		0.10	3.02	0.27	<0.074		<0.009		1.00		0.04	2.88	0.08	0.003		1.25		0.11	2.73	0.16	
159	Tb	<0.002		0.117		0.010	0.318	0.041	<0.007		0.001		0.110		0.012	0.312	0.023	<0.0039		0.142		0.008	0.313	0.018	
163	Dy	<0.010		0.532		0.088	1.61	0.14	<0.057		0.010		0.552		0.021	1.54	0.07	0.018		0.709		0.030	1.43	0.14	
165	Ho	<0.001		0.089		0.015	0.257	0.029	0.005	0.0025	0.001	0.000	0.082		0.001	0.248	0.011	0.002		0.108		0.009	0.230	0.030	
167	Er	0.005		0.223		0.028	0.619	0.063	<0.034		<0.006		0.217		0.029	0.571	0.015	<0.012		0.270		0.012	0.537	0.027	
169	Tm	<0.003		0.030		0.004	0.079	0.012	0.009	0.0045	0.002	0.000	0.029		0.007	0.077	0.004	<0.003		0.032		0.002	0.067	0.017	
173	Yb	0.004		0.193		0.010	0.462	0.083	0.023	0.014	0.006		0.170		0.003	0.482	0.037	<0.017		0.225		0.018	0.477	0.069	
175	Lu	0.001	0.001	0.023		0.006	0.059	0.007	<0.008		0.001	0.001	0.027		0.002	0.081	0.004	<0.002		0.025		0.003	0.053	0.008	
177	Hf	0.004	0.002	0.492		0.101	2.14	0.20	0.131	0.078	<0.009		0.270		0.025	1.44	0.03	0.050	0.003	0.516		0.027	1.74	0.06	
181	Ta	<0.002		0.001		0.000	0.349	0.057	0.296	0.020	0.002	0.000	0.001		0.001	0.167	0.003	0.144	0.016	0.003		0.001	0.294	0.024	
182	W	0.009		0.008		0.003	0.682	0.162	0.119	0.006	0.009		0.005			0.080	0.033	0.029	0.010	0.007		0.000	0.732	0.248	
208	Pb	0.019	0.003	0.895		0.220	3.01	0.42	2.495	0.035	0.027	0.012	0.732		0.041	1.74	0.06	3.60	0.64	1.02		0.09	3.21	0.26	
232	Th	0.002	0.000	0.216		0.039	1.34	0.09	0.002		0.004	0.003	0.047		0.003	0.479	0.066	0.003	0.003	0.317		0.027	1.34	0.13	
238	U	0.002	0.001	0.092		0.015	0.412	0.078	0.006	0.001	0.003	0.002	0.018		0.005	0.096	0.026	0.003	0.003	0.136		0.012	0.518	0.073	

For element concentration data where no corresponding 1sd value is given, there was only one significant spot measurement; hence, these concentrations have to be considered as maximum values.

Table 2

Solution-based $\delta^{11}\text{B}$ for olivine and clinopyroxene separates and reference PRG amphibole. For the latter, *in-situ* results are also shown.

	MC-ICP-MS		LA-MC-ICP-MS		
	$\delta^{11}\text{B}$ (‰)	2 σ (‰)	$\delta^{11}\text{B}$ (‰)	2 σ (‰)	
FAD1 - ol	-5.51	0.01	nd		
FAD2 - cpx	-1.31	0.28	nd		
			N = 12		
PRG	-16.58	0.06	-25.4	2.1	Normalized to NIST SRM612
			-15.9	1.6	Normalized to BHVO-2g

In-situ $\delta^{11}\text{B}$ for PRG amphibole are reported normalized to NIST SRM612 and BHVO-2g (see text for details).

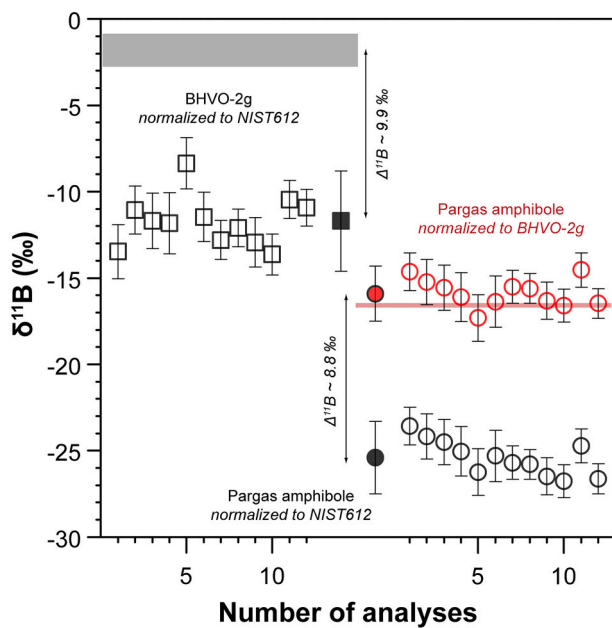


Fig. 4. *In-situ* $\delta^{11}\text{B}$ analyses for the USGS BHVO-2g basaltic glass (squares) and for the Pargas amphibole (circles) normalized to the NIST612 glass (black colour; error bars are 2SE). Red circles are Pargas amphibole analyses normalized to the BHVO-2g glass. Filled symbols are average data $\pm 2\text{SD}$. Reference values for the BHVO-2g (He et al., 2020) and for the Pargas amphibole (this study) are reported with the gray and red area, respectively. Dataset is reported in the Supplementary Table A4. See text for further details. (For interpretation of the references to colour in this figure legend, the reader is referred to the web version of this article.)

separates is always negative (Table 4), ranging between -22.7 and -20.0 ‰ for olivine and clinopyroxenes, and from -14.2 to -12.6 ‰ for phlogopite and amphibole (Fig. 6C).

5.4. Raman spectroscopy characterization of inclusions

Representative Raman spectra of the inclusions hosted within the olivine from harzburgite FAD1 and within the clinopyroxene of sample FAD2 are reported in Fig. 7. In olivine, several inclusions ranging between 2 and 10 μm in size are characterized by infilling of both carbonates and graphite (Fig. 7A). Carbonates show dominant peaks at ca. 1083 and 1098 cm^{-1} , which are compatible with Ca-carbonate and dolomite, respectively. Graphite inclusions in both olivine and clinopyroxene (Fig. 7A, B) show common first-order D1 peak at 1345–1350 cm^{-1} and G peak at ca. 1580 cm^{-1} and the second-order region as well-defined S1 band at 2684–2698 cm^{-1} . Remarkably, these graphitic C

Table 3

B content estimate and $\delta^{11}\text{B}$ of amphibole from FAD1, FFR and FAD2 samples.

Sample	B (ppm)	$\delta^{11}\text{B}$ (‰)	2SE (‰)
FAD1	2.0	-4.3	2.4
	1.9	-4.8	2.1
	2.0	-4.5	2.3
	1.7	-5.5	2.4
	1.9	-1.8	1.6
	1.7	-3.3	2.1
	2.3	-8.2	2.1
	2.4	-6.5	2.5
		mean	2 σ (‰)
		-4.9	3.9
FFR	2.2	-9.4	3.1
	1.2	-8.2	2.0
	1.7	-4.1	1.5
	1.7	-4.0	2.4
		mean	2 σ (‰)
		-6.5	5.6
FAD2	2.1	-4.2	1.7
	2.3	-3.6	1.9
	2.1	-6.1	2.3
	2.6	-5.1	2.7
	2.4	-4.9	2.1
	2.4	-8.2	2.4
		mean	2 σ (‰)
		-5.3	3.3
		mean all data	2 σ (‰)
		-5.4	4.1

B content estimated using the ^{11}B signal ratio between amphibole and BHVO-2g bracketing standard at the LA-MC-ICP-MS.

SE: standard error.

σ : standard deviation.

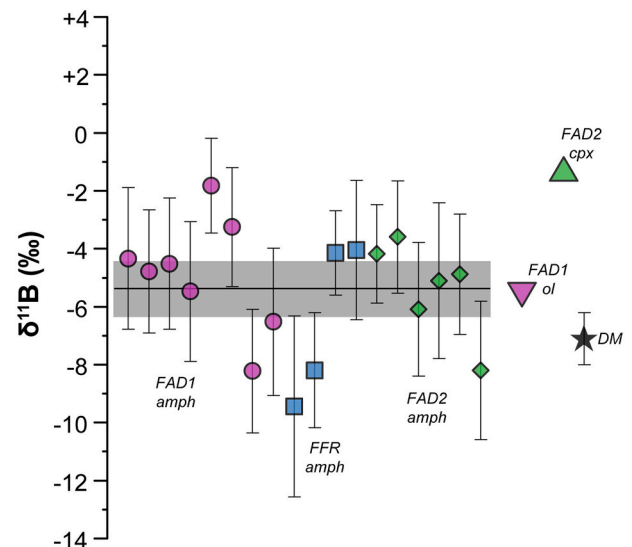


Fig. 5. *In-situ* $\delta^{11}\text{B}$ analyses of amphiboles (amph, error bars are 2SE) and bulk results for olivine (ol) and clinopyroxene (cpx) separates (error within symbols). Black line and gray bar represent amphibole mean value and its 2SE ($n = 18$), respectively. Depleted mantle (DM) value from Marschall et al. (2017).

spectra are diagnostic of well-crystallized structure (Beyssac et al., 2004) suggesting high- T stabilization of the graphite inclusions supporting its primary nature within both olivine and clinopyroxene. Hosted in the olivine grain of the harzburgite FAD1 we detected a peak at 2329 cm^{-1} (Fig. 7C), which is compatible with the wavenumber of molecular N, coexisting with secondary hydrous silicates as evidenced by the presence of their characteristic peaks in the OH region for lizardite and chlorite, between 3600 and 3750 cm^{-1} (Fig. 7C).

Table 4

Carbon and nitrogen content (in ppm) and C isotope composition of the mineral separates of the Finero Phlogopite Peridotite.

		[C] ppm			$\delta^{13}\text{C}$	[N] ppm			
			550 °C	900 °C		<i>meas</i>	<i>corr</i>	550 °C	900 °C
FAD1	ol	268	48	10	−22.7	11	25	<i>bdl</i>	<i>bdl</i>
	phl	686	–	–	−12.6	20	46	–	–
FFR	ol	256	89	8	−20.0	17	39	<i>bdl</i>	<i>bdl</i>
	cpx	601	–	–	−20.0	18	41	–	–
	amph	336	–	–	−14.8	7	16	–	–
	phl	344	183	9	−14.2	10	23	<i>bdl</i>	<i>bdl</i>
FAD2	cpx	273	120	5	−21.3	10	23	<i>bdl</i>	<i>bdl</i>

ol: olivine; cpx: clinopyroxene; amph: amphibole; phl: phlogopite.

bdl: below the detection limit.

meas: measured value at the Elemental Analyzer.

corr: corrected value (see text for details).

6. Discussion

6.1. New evidence of crustal metasomatism

6.1.1. Insights from trace element distribution

Data from our study show that both recrystallized olivine and metasomatic minerals are characterized by significant enrichment in incompatible elements with crustal affinities (Fig. 3), in agreement with previous works. According to the model provided by Zanetti et al. (1999) for the FPP, the clinopyroxenes from the apatite-free harzburgites are in equilibrium with an andesitic-dacitic melt with geochemical signatures closer to those of slab-derived melts (Rapp et al., 1991). During harzburgite impregnation, the melt will start to dissolve olivine that recrystallizes together with spinel + orthopyroxene + clinopyroxene as *T* decreases. The reaction results in an increase of the volatiles content in the melt (mainly H₂O + CO₂) leading to the later stabilization of amphibole and phlogopite mainly along olivine grain boundaries.

To establish if amphibole, clinopyroxene and phlogopite crystallized in chemical equilibrium from the same parental metasomatic agent, we calculated the REE and incompatible element partition coefficients for amphibole/clinopyroxene ($D_{\text{Amph/Cpx}}^{\text{Phl}}$) and phlogopite/amphibole ($D_{\text{Phl/Amph}}^{\text{Cpx}}$), respectively, in harzburgites (Fig. 8). The calculated $D_{\text{REE}}^{\text{Amph/Cpx}}$ are in the range of 3.7–2.8 in the harzburgites and only slightly lower in the clinopyroxenite sample (Fig. 8A). Values are slightly higher than expected at conditions close to chemical equilibrium (Adam and Green, 2006; Ionov et al., 1997; Ionov and Hofmann, 1995; Vannucci et al., 1995) and this is consistent with the early crystallization of clinopyroxene relative to amphibole (Zanetti et al., 1999). The marked enrichment in LREE over HREE of the clinopyroxenes and amphiboles from the harzburgites (Fig. 3A, C), overlapping with the data from the apatite-free domain from Zanetti et al. (1999), suggests that the mantle samples experienced metasomatism by volatile-bearing and silicate-rich melts, potentially deriving from a dehydrating subducted slab (Zanetti et al., 1999). Textural evidence suggests that amphibole and phlogopite, which both represent the most evident result of the metasomatism within the FPP, are in equilibrium (Fig. 2A, B). The patterns of the $D_{\text{Amph/Cpx}}^{\text{Phl}}$ of the FPP harzburgites (Fig. 8B) mimic those of natural metasomatized mantle rocks and experiments in ultramafic systems where phlogopite and amphibole are in chemical equilibrium (Adam and Green, 2006; Grégoire et al., 2000; Moine et al., 2001; Scambelluri et al., 2006), thus supporting their coeval crystallization from the same metasomatic agent. Texture and chemical signatures suggest that amphibole, clinopyroxene and phlogopite from the harzburgites and the clinopyroxenite vein (Fig. 3) likely crystallized from the same metasomatic agent in a continuum process. The mismatch in several trace element enrichments (e.g., La, Th, U and W) between the clinopyroxenes and the amphiboles of the two harzburgites (Fig. 3A–D) appear to be related to the proximity of the clinopyroxene vein (sample FAD2), which acted as preferential channel-way during the hydrous melt percolation.

Previous works aimed to unravel the metasomatic history of the FPP

and, more in general, to disclose mantle metasomatism, have shown that light lithophile elements (LLE – Li, Be and B) may be used as powerful tracers of such a process (Bebout et al., 1999; Ottolini et al., 2004; Raffone et al., 2006; Ryan et al., 1996). As shown in Fig. 9, Ce/B and Li/Yb ratios in clinopyroxene from the FPP harzburgites and clinopyroxenite depart from common LLE signature of sub-continental depleted mantle trending towards more enriched signatures approaching the field of volcanic arc composition. The most enriched rocks are located in major shear zone within the FPP (Corvò et al., 2020). These enrichments in Li and B are consistent with an overprinting of the uncontaminated mantle geochemistry through the interaction with subduction-related melts (Raffone et al., 2006). More likely, the trend observed in Fig. 9, with variable enrichment in B and Li over Ce and Yb, together with the enrichments in other fluid-mobile elements such as As and Sb in recrystallized olivine (Fig. 3E), rather point to the record of the metasomatic imprint.

6.1.2. Insights from C and N

The high concentrations in incompatible elements shown by the rock-forming silicates constituting the FPP (Fig. 3) are coupled with high levels of C and N as envisaged by the mineral separates bulk concentrations reported in this study. Remarkably, these volatiles are commonly stored in surficial reservoirs (i.e., atmosphere, organic materials, sediments and altered rocks) suggesting that the metasomatic agent interacting with the FPP derived from recycled material and likely from a subducting slab. The positive correlation shown by C and N (Fig. 6B) indicates that these elements might be genetically related. Noteworthy, the [C]₅₅₀ data reported in this study suggest that up to 80% of the initial C is lost from the silicates (Fig. 6A) indicating that significant amount of the initial C was present in its reduced form (i.e., graphite), that is easily converted to CO₂ and extracted from the minerals at *T* of 550 °C. The [C] data obtained after heating mineral powders overnight at 900 °C point to a 96% loss of the initial C suggesting that the remaining C was mostly present as carbonates that are likely removed from the sample at *T* higher than 800 °C. This evidence is in strong agreement with the occurrence of both graphite- and carbonate-bearing inclusions hosted within the olivine and clinopyroxene of sample FAD1 and FAD2 (Fig. 7A, B), respectively. The coexistence of both graphitic C and carbonate in inclusions (Fig. 7A, B) points to redox conditions approaching the C-CO/CO₂ equilibrium during the metasomatic process, as also reported in the previous work of Ferraris et al. (2004). At 550 °C the [N] is already below the detection limits suggesting that N is unlikely entrapped as N-bearing mineral inclusions or in the crystal structures of the minerals (in phlogopite) and is mainly related to the presence of fluid/gaseous inclusions. This is supported by the occurrence of molecular N₂ coexisting with hydrous silicates (chlorite and lizardite) in olivine crystals (Fig. 7C) which is interpreted to represent the result of the interaction between the host olivine and the entrapped fluid. The inclusion was mainly filled by N-bearing aqueous fluid where the N was likely in the form of NH₄⁺, which is expected to be the

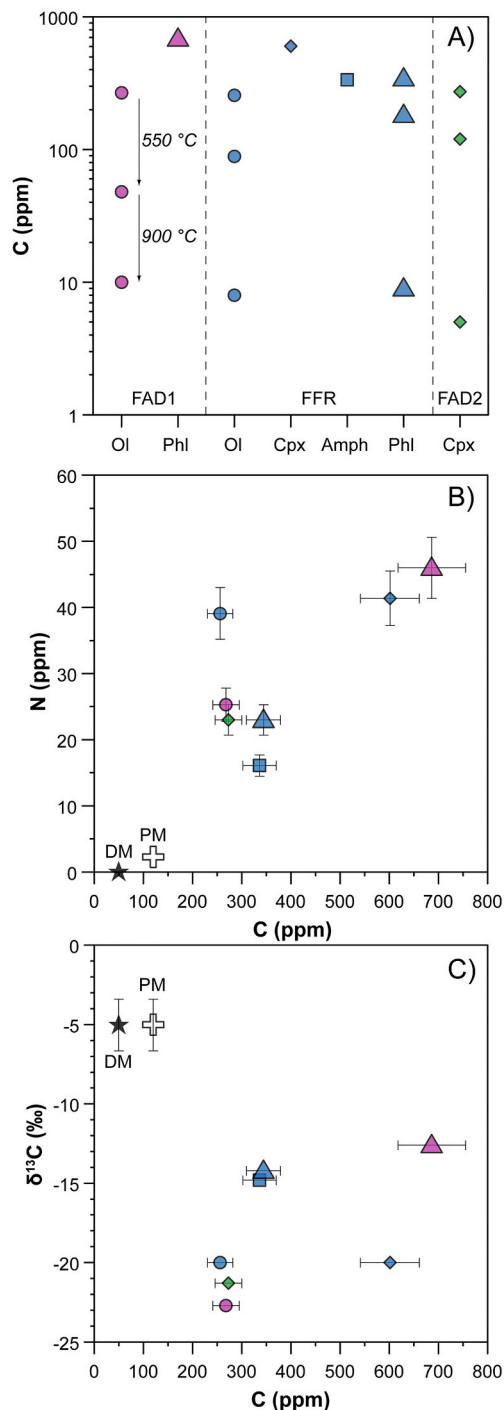


Fig. 6. (A) C concentrations ([C]) for untreated and treated (at 550 and 900 °C) mineral separates (see Table 4). (B) Relationship between [C] and [N] of untreated minerals. Note that [N] are considered minimum values (see text for details). PM and DM are primitive and depleted mantle, respectively (McDonough and Sun, 1995; Salters and Stracke, 2004). (C) $\delta^{13}\text{C}$ vs. [C] of untreated minerals.

dominant N form at upper mantle conditions (Mikhail and Sverjensky, 2014), although it can be present directly as N_2 in supra-subduction settings (Mysen, 2019). In the former case, the interaction process between the host and the fluid inclusion leads to the hydration of the olivine with the consequent formation of secondary chlorite and lizardite that, coupled with potential leakage of H^+ out of fluid inclusions by diffusion, leaves molecular N_2 . The invoked process of leakage of H^+

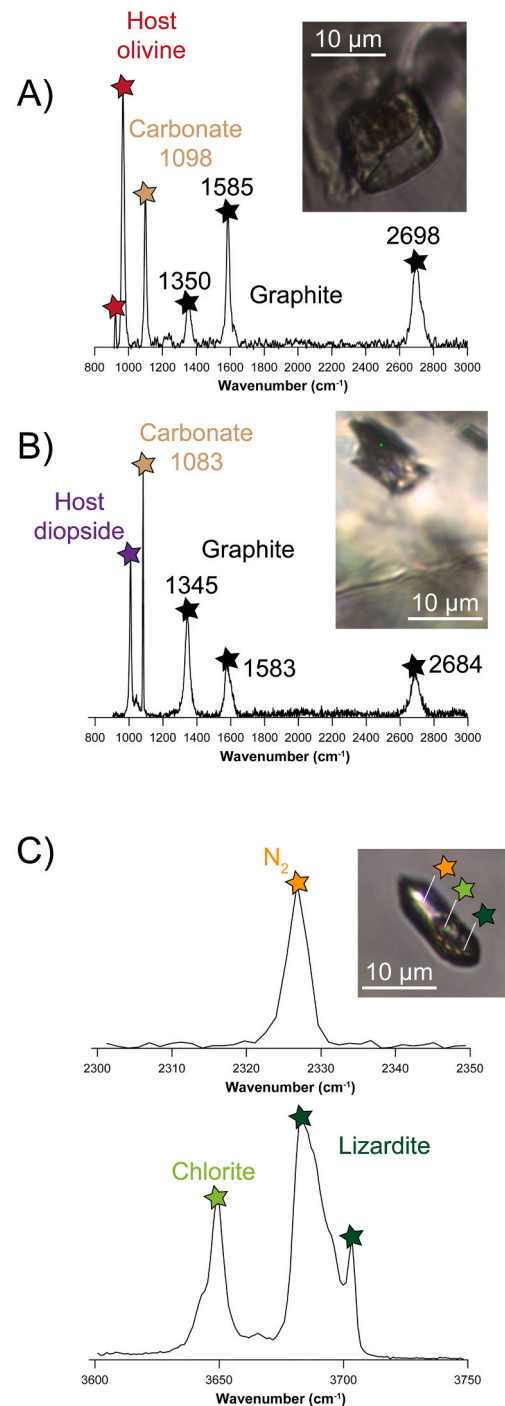


Fig. 7. Micro-Raman spectra of the investigated solid inclusions reported in the inset and hosted in olivine from sample FAD1 (A and C) and in diopside from sample FAD2 (B).

out of the fluid inclusions is advocated for noble gas and N retention in high-*P* ultramafic rocks (Halama et al., 2014; Kendrick et al., 2011).

6.2. New isotopic constrain for the subduction-related origin of the metasomatic agent

6.2.1. Boron isotope signature

Compared to common mantle derived rocks (Marschall et al., 2017), harzburgites and clinopyroxenite vein from the FPP are significantly enriched in B. Boron is a FME and its isotopic signature is a powerful

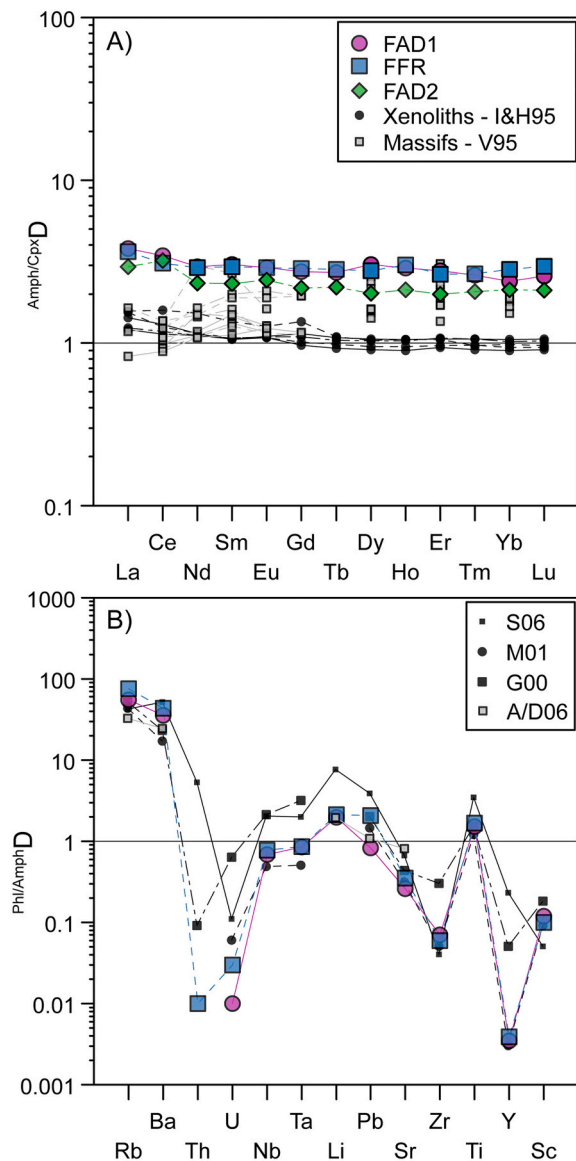


Fig. 8. (A) Calculated amphibole/clinopyroxene partition coefficients ($D^{Amph/Cpx}$) for REEs compared to literature data from xenoliths (Ionov and Hofmann, 1995) and massifs (Vannucci et al., 1995). (A) Calculated $Phl/AmphD$ s for key elements (LILEs, HFSE, actinide, Pb) for harzburgites compared with natural and experimental data from the literature (S06: Scambelluri et al., 2006; M01: Moine et al., 2001; G00: Grégoire et al., 2000; A/D06: Adam and Green, 2006). (For interpretation of the references to colour in this figure legend, the reader is referred to the web version of this article.)

geochemical tracer of subduction-related processes (De Hoog and Savov, 2018). Hydrated oceanic lithosphere is enriched in B relative to the mantle and possesses a $\delta^{11}B$ signature deviating from that of the uncontaminated mantle ($\delta^{11}B \sim -7.1\%$, Marschall et al., 2017) towards positive values due to alteration by seawater-derived fluids (with a present-day $\delta^{11}B$ of $\sim +39.6\%$). Prograde subduction dehydration of the altered oceanic crust and of the sediments laying atop leads to a preferential ^{11}B enrichment in the released fluids and ^{11}B -poor slabs that will show negative $\delta^{11}B$ imprint at depth of 90–120 km (Rosner et al., 2003; Tonarini et al., 2011). On the contrary, hydrated ultramafic mantle from the slab and the forearc region likely preserves its positive $\delta^{11}B$ imprint down to sub-arc condition, where antigorite dehydration provides ^{11}B -rich fluids (Tonarini et al., 2011; Konrad-Schmolke and Halama, 2014; Cannaò, 2020). The $\delta^{11}B$ values reported here for olivine,

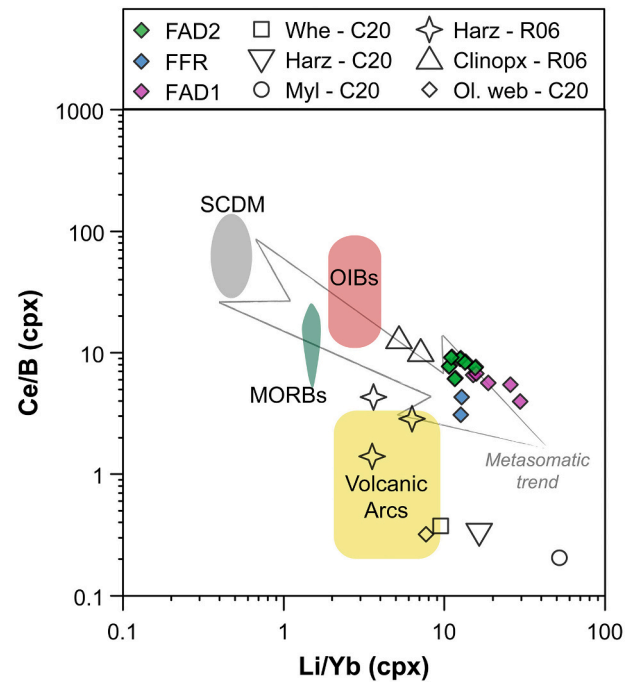


Fig. 9. Ce/B vs. Li/Yb ratios showing the metasomatic evolution in clinopyroxene (gray arrow; after Raffone et al., 2006). SCDM: sub-continental depleted mantle from Ottolini et al. (2004); OIBs: oceanic island basalts, MORBs: middle oceanic ridge basalts and volcanic arcs fields are from Ryan et al. (1996); Ryan and Langmuir (1987, 1993). R06: Raffone et al. (2006); C20: Corvò et al. (2020).

clinopyroxene and amphiboles of the FPP are mostly higher than those characterizing the depleted mantle and thus the involvement of a ^{11}B -rich reservoir(s) is required. The B isotopic signature of the analyzed minerals mimic that of the residual slab generated deeply in subduction zones and contaminated by serpentinite-derived fluids (Fig. 10). Remarkably, comparable negative $\delta^{11}B$ values are documented in olivine and amphibole (plus phlogopite) from veins hosted in mantle xenoliths from the Kamchatka arc (Tomanikova et al., 2019). Their $\delta^{11}B$ signatures are mainly interpreted as the products of melts released from ^{11}B -depleted oceanic slab coupled with minor and variable amount of ^{11}B -rich reservoir, such as serpentinite-derived fluids (Fig. 10). Considering that B in amphibole is highly incompatible ($D^{Amph/Melt}_{DB} \sim 0.006$ – 0.100 ; Cannaò et al., 2022; Tiepolo et al., 2007), the B concentration of the residual slab melt should range between 35 and 500 ppm ($1/B \sim 0.002$ – 0.03 in Fig. 10). This range agrees with the B concentrations of 134.4 ppm calculated for residual slab melts considering a residual slab with ca. 16.8 ppm of B (Tonarini et al., 2011) and a $D^{Melt/rock}_{DB}$ of 8 (Kessel et al., 2005; see Supplementary Table A5 for mixing model input parameters). The $\delta^{11}B$ of the FPP minerals analyzed in this study can be achieved by adding up to 30% of ^{11}B -rich component (likely from serpentinite-derived fluids) to the estimated residual slab melt. According to the model, about 3% of the calculated mixed component is required to shift the $\delta^{11}B$ of depleted mantle towards values overlapping those of amphiboles, olivine and clinopyroxene of the FPP. The involvement of slab-deriving materials in the genesis of the amphibole of the FPP is also supported by their trace element budget showing enrichments in LREE and other incompatible elements (Fig. 3C, D) that are mobilized during melting of crust, as documented in high-*P* experiments (Kessel et al., 2005). Noticeably, the required contribution of slab-derived component is also within the upper limit of 10% suggested by Zanetti et al. (1999) to explain the trace element budget of the FPP.

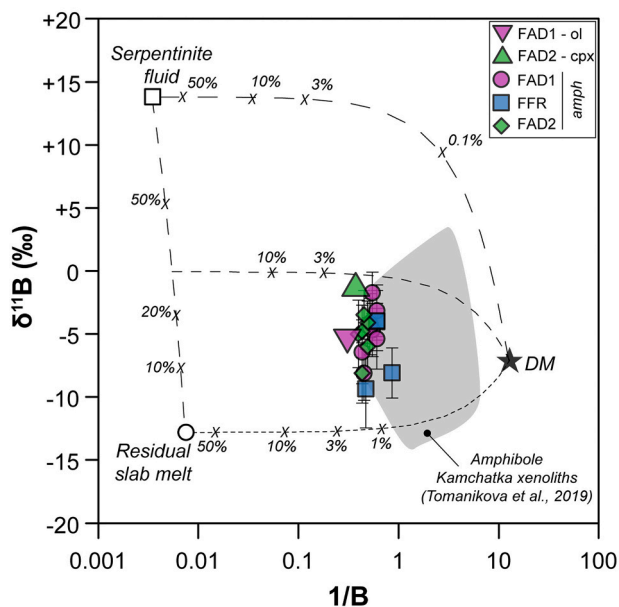


Fig. 10. $1/B$ vs. $\delta^{11}B$ of the amphiboles (errors are 2SE), olivine and clinopyroxene of the FPP. The diagram shows two major mixing trends between depleted mantle (DM, [Marshall et al., 2017](#)) and slab-derived melt (fine dashed line) and serpentinite fluids (coarse dashed line) reservoirs formed at 120 km depth. Mixing model input parameters are reported in the Supplementary Table A5. The model suggests that ca. 3% of composite hydrous melt made of residual slab melt and up to 30% of serpentinite-derived fluid is required to match the $\delta^{11}B$ signatures reported for the FPP. The numbers indicate the percentage of the residual slab component added to the mantle source. Gray field reports range for amphibole from veined mantle xenoliths from the Kamchatka arc ([Tomanikova et al., 2019](#)). See text for details.

6.2.2. Carbon isotope signature

The C isotope composition of mantle xenoliths is bimodal with a $\delta^{13}C$ dominant peak at $-5 \pm 2\text{‰}$ and a minor secondary peak at $\sim -25\text{‰}$ ([Deines, 2002](#)). The less negative $\delta^{13}C$ signature has been identified as that characteristic of the Earth's mantle, whereas the more negative values are mainly suggested to reflect mantle-derived rocks contaminated by ^{12}C -rich materials from recycled crustal sources ([Deines, 2002](#)). Remarkably, the $\delta^{13}C$ of worldwide diamonds ([Cartigny et al., 2014](#)) overlaps the bimodal $\delta^{13}C$ signatures of mantle xenoliths suggesting a genetic interconnection. However, this topic is still a matter of debate in the scientific community (e.g., [Cartigny et al., 2014](#)). The C isotope composition of the mineral separates of the FPP shows a ^{13}C -depleted imprint ranging between -12.6 to -22.7‰ (Table 4), values that significantly depart from the predominant Earth's mantle signature and partially overlap the ^{12}C -rich component of the mantle. Noticeably, olivine and clinopyroxene have the most negative $\delta^{13}C$ values (Table 4, Fig. 4C) that we interpret as related to the dominant presence of ^{12}C -rich graphite inclusions as detected by micro-Raman investigations (Fig. 5). Although the occurrence of carbonate inclusions has been documented (Fig. 5A, C), if we consider that up to 82% of graphitic C is lost from olivine of sample FAD1 after heating at 550 °C , we can reasonably assume that the measured $\delta^{13}C$ value of -22.7‰ mostly reflect the C isotope composition of the graphite. By using the C isotope fractionation between CO_2 and graphite ([Scheele and Hoefs, 1992](#)) at T of 700 – 900 °C , consistent with the thermic conditions experienced by the FPP during metasomatic processes ([Ferraris et al., 2004](#); [Tommasi et al., 2017](#)), we calculate a $\Delta^{13}C_{CO_2\text{-graphite}}$ of $+7.8$ to $+6.3\text{‰}$, respectively. The calculated CO_2 in equilibrium with the graphite has a $\delta^{13}C$ ranging from -16.4 to -14.9‰ , lower than the typical values for mantle-derived magmatic CO_2 of -10 to -7‰ ([Kelley and Früh-Green, 1999](#)). This suggests the involvement of a ^{12}C -rich material(s) in the source of the metasomatized agent of the FPP. Similar results were documented by

[Zhang et al. \(2007\)](#) for the metasomatized SCLM beneath eastern China, where the $\delta^{13}C_{CO_2}$ values ranging between -15 and -28‰ were related to recycled crustal volatiles from oceanic crust and terrigenous sediments. Light C isotope compositions from -26 to -16‰ for graphite-bearing ultramafic rocks are also shown in the graphite-sulfide deposits from the Ronda and Beni Bousera massifs ([Crespo et al., 2006](#)). Here, the light $\delta^{13}C$ signatures are accounted by an exogenous C recycled to depth via subduction processes. The formation of olivine and clinopyroxene hosting graphite with a ^{12}C -enriched composition led to an evolved ^{13}C -enriched residual hydrous melt that percolating along the olivine grain boundaries, crystallized amphibole and phlogopite. In this scenario, amphibole and phlogopite are expected to show less negative $\delta^{13}C$ imprint than those of the olivine and clinopyroxene. The $\delta^{13}C$ signatures of amphibole and phlogopite (from -14.8 to -12.6‰ ; Fig. 4C, Table 4) are consistent with the above scenario supporting a single and continuous metasomatic event. All together, these geochemical evidences concur on a subduction-like environment for the metasomatic process affecting the FPP.

6.3. Implications for the global C cycle

Carbon cycle on our planet is neither a steady-state nor a globally averaged process ([Plank and Manning, 2019](#)). Global mass balance calculations suggest, although with a large uncertainties, an imbalance between the amount of C in and out of the mantle ([Kelemen and Manning, 2015](#)), thus calling for a *hidden C reservoir(s)*. Candidates are the forearc and subarc mantle regions, the lithospheric mantle and the deep crust ([Kelemen and Manning, 2015](#); [Scambelluri et al., 2016](#)).

The trace elements and $\delta^{11}B$ investigations resulting from this study together with literature data have shown that the FPP rocks represent an upper mantle section affected by significant enrichment in relation to metasomatic processes likely involving slab-derived melts. Moreover, in agreement with the abundant crystallization of hydrous phases (amphibole and phlogopite) and the high whole-mineral C and N concentrations, suggest that the metasomatic agent was rich in volatile. Further support is also given by C–N inclusions entrapped into olivine and clinopyroxene.

This work has shown that C and N are mainly entrapped as inclusions in the FPP minerals and this agrees with the evidence that their concentrations are several orders of magnitude higher than those commonly shown by anhydrous silicates ([Keppler et al., 2003](#); [Li et al., 2013](#); [Rosenthal et al., 2015](#); [Shcheka et al., 2006](#)) that dominate the upper mantle mineral assemblage ([Stixrude and Lithgow-Bertelloni, 2007](#)). Notwithstanding, the C and N enrichments in the studied rocks point to a not negligible role of the fluid induced mantle metasomatism in the mantle wedge in storing volatiles in the SCLM at depth in the form of inclusions in metasomatic minerals. The residence time and long-term fate of this C is poorly known, and its quantification is challenging ([Kelemen and Manning, 2015](#)). However, C fixed as inclusions in metasomatic minerals on long geological timescales may have a significant impact on the deep global C cycle. Detachment and sinking of the lower parts of the SCLM due to density-driven delamination (e.g., [Caracausi and Sulli, 2019](#); [Elkins-Tanton, 2007](#); [Kay and Kay, 1993](#)) is envisaged as a prominent process able to remobilize volatiles. It is important to note that, despite the partial loss of C after sample treatment at medium and high- T , a residual C content is still hosted in clinopyroxene, phlogopite and olivine in amounts from 5 to 10 ppm (Fig. 4A; Table 4). These concentrations are significantly higher compared to the C solubility documented by experimental works for C-free silicates at upper mantle conditions ([Keppler et al., 2003](#); [Rosenthal et al., 2015](#); [Shcheka et al., 2006](#)), suggesting that low- to medium- T processes are virtually not strong enough to extract all C. In this context, the metasomatized SCLM might contribute to the so-called *hidden C reservoir* invoked to match the global C mass balance calculations ([Kelemen and Manning, 2015](#)).

7. Conclusions

In this study, we provide petrographic and geochemical constraints regarding the incorporation of C and N within rock-forming minerals of a strongly metasomatized sector of the sub-continental lithospheric mantle (SCLM), namely the Finero phlogopite-bearing peridotite (FPP; Ivrea-Verbano Zone). The main results of our work can be summarized as follows:

- *In-situ* LA-ICP-MS trace elements investigation confirms that the metasomatic process affecting the FPP derive from a hydrous melt with crustal affinity likely occurring as a single and progressive event.
- The enrichment in incompatible trace elements is coupled with high levels of C and N, suggesting that the metasomatic agent was enriched in volatiles. The micro-Raman investigation documents the occurrence of both graphite and carbonates inclusions in olivine and clinopyroxene. Gaseous N₂ is present as inclusions in olivine too. The occurrence of such inclusions is likely responsible for the high C–N concentrations reported in the analyzed mineral separates.
- The $\delta^{13}\text{C}$ as low as -22.7‰ reported for olivine and clinopyroxene reflects an overprinting of the common C mantle signature, pointing to a C contamination from a ^{12}C -rich crustal metasomatic agent. The ^{13}C -enriched isotope composition of amphibole and phlogopite (up to -12.6‰) is compatible with the proposed single-stage metasomatic process accordingly with the trace element composition.
- The negative $\delta^{11}\text{B}$ at $-5.4 \pm 4.1\text{‰}$ (2σ , $n = 18$) reported for amphibole *via in-situ* LA-MC-ICP-MS analyses and of $-5.51 \pm 0.01\text{‰}$ (2σ) and $-1.82 \pm 0.06\text{‰}$ (2σ) obtained for olivine and clinopyroxene, respectively, with MC-ICP-MS require the involvement of ^{11}B -rich slab. This component fits with residual slab melts coupled with variable amounts of ^{11}B -rich reservoir, such as serpentinite-derived fluids.
- High-*T* decarbonation process, simulated by heating the samples at 900 °C , suggests that 5 to 10 ppm of C can be stored in the SCLM, whereas N is expected to be completely released even at lower *T* if it is incorporated in inclusions. Nitrogen structurally incorporated in minerals (e.g., NH₄ in micas and clinopyroxene; Halama et al., 2017; Watenphul et al., 2010) is expected to be stored in the SCLM until their destabilization.

Our results support the scenario that inclusions in the metasomatic minerals in the SCLM might acts as *hidden C reservoir*, thus playing an important role for its storage on long geological timescales.

Declaration of Competing Interest

The authors declare that they have no known competing financial interests or personal relationships that could have appeared to influence the work reported in this paper.

Data availability

Data will be made available on request.

Acknowledgements

The “Museo delle Collezioni Mineralogiche” of the Earth Science Department “A. Desio”, University of Milano LA STATALE is warmly acknowledged for providing the amphibole from the Pargas locality. This work benefits funding from the Italian Ministry of Education, University and Research (MIUR) – Excellent Departments Projects. Boron isotope analyses on bulk minerals were partially supported by IGG-CNR fund P1600514. The authors are grateful to R. Halama and T. Morishita for the constructive comments that improved the quality of the manuscript.

Appendix A. Supplementary data

Supplementary data to this article can be found online at <https://doi.org/10.1016/j.chemgeo.2022.121181>.

References

- Adam, J., Green, T., 2006. Trace element partitioning between mica- and amphibole-bearing garnet lherzolite and hydrous basaltic melt: 1. Experimental results and the investigation of controls on partitioning behaviour. *Contrib. Mineral. Petrol.* 152, 1–17. <https://doi.org/10.1007/s00410-006-0085-4>.
- Agostini, S., di Giuseppe, P., Manetti, P., Doglioni, C., Conticelli, S., 2021. A heterogeneous subcontinental mantle under the African–Arabian Plate boundary revealed by boron and radiogenic isotopes. *Sci. Rep.* 11 <https://doi.org/10.1038/s41598-021-90275-7>.
- Baldwin, S.L., Schöning, J., Gonzalez, J.P., Davies, H., von Eynatten, H., 2021. Garnet sand reveals rock recycling processes in the youngest exhumed high- and ultrahigh-pressure terrane on Earth. *Proc. Natl. Acad. Sci. U. S. A.* 118 <https://doi.org/10.1073/pnas.2017231118>.
- Barry, P.H., Hilton, D.R., 2016. Release of subducted sedimentary nitrogen throughout Earth's mantle. *Geochem. Perspect. Lett.* 148–159 <https://doi.org/10.7185/geochemlet.1615>.
- Barry, P.H., de Moor, J.M., Giovannelli, D., Schrenk, M., Hummer, D.R., Lopez, T., Pratt, C.A., Segura, Y.A., Battaglia, A., Beaudry, P., Bini, G., Cascante, M., d'Errico, G., di Carlo, M., Fattorini, D., Fullerton, K., Gazel, E., González, G., Halldórsson, S.A., Iacovino, K., Kulonogski, J.T., Manini, E., Martínez, M., Miller, H., Nakagawa, M., Ono, S., Patwardhan, S., Ramírez, C.J., Regoli, F., Smedile, F., Turner, S., Vetriani, C., Yücel, M., Ballentine, C.J., Fischer, T.P., Hilton, D.R., Lloyd, K.G., 2019. Forearc carbon sink reduces long-term volatile recycling into the mantle. *Nature* 568, 487–492. <https://doi.org/10.1038/s41586-019-1131-5>.
- Bebout, G.E., 2014. 4.20 - chemical and isotopic cycling in subduction zones. In: Turekian, H.D.H.K. (Ed.), *Treatise on Geochemistry*, Second edition. Elsevier, Oxford, pp. 703–747.
- Bebout, G.E., Ryan, J.G., Leeman, W.P., Bebout, A.E., 1999. Fractionation of trace elements by subduction zone metamorphism effect of convergent margin thermal evolution. *Earth Planet. Sci. Lett.* 171, 63–81.
- Beyssac, O., Brunet, F., Petit, J.-P., Goffé, B., Rouzaud, J.-N., 2004. Experimental study of the microtextural and structural transformations of carbonaceous materials under pressure and temperature. *Eur. J. Mineral.* 15, 937–951. <https://doi.org/10.1127/0935-1221/2003/0015-0937>.
- Boocock, T.J., Mikhail, S., Prytulak, J., Di Rocco, T., Stüeken, E.E., 2020. Nitrogen mass fraction and stable isotope ratios for fourteen geological reference materials: evaluating the applicability of elemental analyser versus sealed tube combustion methods. *Geostand. Geoanal. Res.* 44, 537–551. <https://doi.org/10.1111/ggr.12345>.
- Busigny, V., Cartigny, P., Laverne, C., Teagle, D., Bonifacie, M., Agrinier, P., 2019. A reassessment of the nitrogen geochemical behavior in upper oceanic crust from Hole 504B: implications for subduction budget in central America. *Earth Planet. Sci. Lett.* 525, 115735 <https://doi.org/10.1016/j.epsl.2019.115735>.
- Bussolati, M., Grieco, G., Tzamos, E., 2019. Olivine–spinel diffusivity patterns in chromitites and dunites from the finero phlogopite-peridotite (Ivrea-Verbano Zone, Southern Alps): implications for the thermal history of the massif. *Minerals* 9. <https://doi.org/10.3390/min9020075>.
- Cannà, E., 2020. Boron isotope fractionation in subducted serpentinites: a modelling attempt. *Lithos* 105768. <https://doi.org/10.1016/j.lithos.2020.105768>.
- Cannà, E., Malaspina, N., 2018. From oceanic to continental subduction: implications for the geochemical and redox evolution of the supra-subduction mantle. *Geosphere* 14, 2311–2336. <https://doi.org/10.1130/GES01597.1/4457636/GES01597.pdf>.
- Cannà, E., Tiepolo, M., Bebout, G.E., Scambelluri, M., 2020. Into the deep and beyond: carbon and nitrogen subduction recycling in secondary peridotites. *Earth Planet. Sci. Lett.* 543, 116328 <https://doi.org/10.1016/j.epsl.2020.116328>.
- Cannà, E., Tiepolo, M., Borghini, G., Langone, A., Fumagalli, P., 2022. The influence of oxygen fugacity and chlorine on amphibole-liquid trace element partitioning at upper-mantle conditions. *Eur. J. Mineral.* 34, 35–57. <https://doi.org/10.5194/ejm-34-35-2022>.
- Caracausi, A., Sulli, A., 2019. Outgassing of mantle volatiles in compressional tectonic regime away from volcanism: the role of continental delamination. *Geochim. Geophys. Geosyst.* 20, 2007–2020. <https://doi.org/10.1029/2018gc008046>.
- Cartigny, P., Marty, B., 2013. Nitrogen isotopes and mantle geodynamics: the emergence of life and the atmosphere-crust-mantle connection. *Elements* 9, 359–366. <https://doi.org/10.2113/gselements.9.5.359>.
- Cartigny, P., Palot, M., Thomassot, E., Harris, J.W., 2014. Diamond formation: a stable isotope perspective. *Annu. Rev. Earth Planet. Sci.* 42, 699–732. <https://doi.org/10.1146/annurev-earth-042711-105259>.
- Catanzaro, F., Champion, C., Garner, E., Marinenko, G., Sappenfield, K., Shields, W., 1970. Boric acid: isotopic and assay standard reference materials. In: National Bureau of Standards (US) Special Publications, 260, pp. 1–70.
- Coltorti, M., 1984. Mantle tectonite and fractionate peridotite at Finero (Italian Western Alps). *Neues Jahrbuch für Mineralogie. Abhandlungen* 149 (3), 225–244.
- Corvò, S., Langone, A., Padrón-Navarta, J.A., Tommasi, A., Zanetti, A., 2020. Porphyroclasts: source and sink of major and trace elements during deformation-induced metasomatism (finero, ivrea-verbano zone, Italy). *Geosciences* (Switzerland) 10. <https://doi.org/10.3390/geosciences10050196>.
- Crespo, E., Luque, F.J., Rodas, M., Wada, H., Gervilla, F., 2006. Graphite-sulfide deposits in Ronda and Beni Bousera peridotites (Spain and Morocco) and the origin of carbon

- in mantle-derived rocks. *Gondwana Res.* 9, 279–290. <https://doi.org/10.1016/j.gr.2005.10.003>.
- Cumming, G.L., Köppel, V., Ferrario, A., 1987. A lead isotope study of the northeastern Ivrea zone and the adjoining Ceneri zone (N-Italy): evidence for a contaminated subcontinental mantle. *Contrib. Mineral. Petrol.* 97, 19–30. <https://doi.org/10.1007/bf00375211>.
- Dasgupta, R., Grewal, D.S., 2019. Origin and Early Differentiation of Carbon and Associated Life-Essential Volatile Elements on Earth.
- De Hoog, J.C.M., Savov, I.P., 2018. Boron isotopes as a tracer of subduction zone processes. *Boron Isot.* 217–247. https://doi.org/10.1007/978-3-319-64666-4_9.
- Dean, W.E., 1974. Determination of carbonate and organic matter in calcareous sediments and sedimentary rocks by loss on ignition; comparison with other methods. *J. Sediment. Res.* 44 (1), 242–248.
- Deines, P., 2002. The Carbon Isotope Geochemistry of Mantle Xenoliths, 58, pp. 247–278.
- Elkins-Tanton, L.T., 2007. Continental magmatism, volatile recycling, and a heterogeneous mantle caused by lithospheric gravitational instabilities. *J. Geophys. Res. Solid Earth* 112. <https://doi.org/10.1029/2005jb004072>.
- Evans, D., Gerdes, A., Coenen, D., Marschall, H.R., Müller, W., 2021. Accurate correction for the matrix interference on laser ablation MC-ICPMS boron isotope measurements in CaCO₃ and silicate matrices. *J. Anal. At. Spectrom.* 36 (8), 1607–1617. ISO 690.
- Ferraris, C., Grobety, B., Früh-Green, G.L., Wessicken, R., 2004. Intergrowth of graphite within phlogopite from Finero ultramafic complex (Italian Western Alps): implications for mantle crystallization of primary-texture mica. *Eur. J. Mineral.* 16, 899–908. <https://doi.org/10.1127/0935-1221/2004/0016-0899>.
- Foster, G.L., 2008. Seawater pH, pCO₂ and [CO₂-3] variations in the Caribbean Sea over the last 130 kyr: a boron isotope and B/Ca study of planktic foraminifera. *Earth Planet. Sci. Lett.* 271, 254–266. <https://doi.org/10.1016/j.epsl.2008.04.015>.
- Fountain, D.M., 1976. The Ivrea-Verbanio and Strona-Ceneri zones, Northern Italy: a cross-section of the continental crust-New evidence from seismic velocities of rock samples. *Tectonophysics*. [https://doi.org/10.1016/0040-1951\(76\)90054-8](https://doi.org/10.1016/0040-1951(76)90054-8).
- Galloway, J.N., Dentener, F.J., Capone, D.G., Boyer, E.W., Howarth, R.W., Seitzinger, S. P., Asner, G.P., Cleveland, C.C., Green, P.A., Holland, E.A., Karl, D.M., Michaels, A. F., Porter, J.H., Townsend, A.R., Vörösmarty, C.J., 2004. Nitrogen cycles: past, present, and future. *Biogeochemistry* 70, 153–226. <https://doi.org/10.1007/s10533-004-0370-0>.
- Gonzalez, C.M., Gorczyk, W., Gerya, T.V., 2016. Decarbonation of subducting slabs: insight from petrological–thermomechanical modeling. *Gondwana Res.* 36, 314–332. <https://doi.org/10.1016/j.gr.2015.07.011>.
- Grégoire, M., Moine, B.N., O'Reilly, S.Y., Cottin, J.Y., Giret, A., 2000. Trace element residence and partitioning in mantle xenoliths metasomatized by highly alkaline, silicate- and carbonate-rich melts (Kerguelen Islands, Indian Ocean). *J. Petrol.* 41, 477–509. <https://doi.org/10.1093/petrology/41.4.477>.
- Grieco, G., Ferrario, A., Von Quadt, A., Koepfel, V., Mathez, E.A., 2001. The zircon-bearing chromitites of the phlogopite peridotite of Finero (Ivrea zone, Southern Alps): evidence and geochronology of a metasomatized mantle slab. *J. Petrol.* 42, 89–101. <https://doi.org/10.1093/petrology/42.1.89>.
- Grieco, G., Ferrario, A., Mathez, E.A., 2004. The effect of metasomatism on the Cr-PGE mineralization in the Finero complex, Ivrea Zone, Southern Alps. *Ore Geol. Rev.* 24, 299–314. <https://doi.org/10.1016/j.oregeorev.2003.05.004>.
- Griffin, W.L., Powell, W.J., Pearson, N.J., O'Reilly, S.Y., 2008. GLITTER: Data Reduction Software for Laser Ablation ICP-MS. *Laser Ablation-ICP-MS in the Earth Sciences*.
- Halama, R., Bebout, G.E., John, T., Scambelluri, M., 2014. Nitrogen recycling in subducted mantle rocks and implications for the global nitrogen cycle. *Int. J. Earth Sci.* 1–19. <https://doi.org/10.1007/s00531-012-0782-3>.
- Halama, R., Bebout, G.E., Marschall, H.R., John, T., 2017. Fluid-induced breakdown of white mica controls nitrogen transfer during fluid–rock interaction in subduction zones. *Int. Geol. Rev.* 59, 702–720. <https://doi.org/10.1080/00206814.2016.1233834>.
- Halama, R., Bebout, G.E., Bea, F., 2021. Nitrogen loss and isotopic fractionation during granulite-facies metamorphism in the lower crust (Ivrea Zone, NW Italy). *Chem. Geol.* 584. <https://doi.org/10.1016/j.chemgeo.2021.120475>.
- Handy, M.R., Franz, L., Heller, F., Janott, B., Zurrbruggen, R., 1999. Multistage accretion and exhumation of the continental crust (Ivrea crustal section, Italy and Switzerland). *Tectonics* 18, 1154–1177. <https://doi.org/10.1029/1999tc900034>.
- Hartmann, G., Hans Wedepohl, K., 1993. The composition of peridotite tectonites from the Ivrea complex, northern Italy: residues from melt extraction. *Geochim. Cosmochim. Acta* 57, 1761–1782. [https://doi.org/10.1016/0016-7037\(93\)90112-A](https://doi.org/10.1016/0016-7037(93)90112-A).
- He, M., Xia, X., Huang, X., Ma, J., Zou, J., Yang, Q., Wei, G., 2020. Rapid determination of the original boron isotopic composition from altered basaltic glass by in situ secondary ion mass spectrometry. *J. Anal. At. Spectrom.* 35 (2), 238–245. ISO 690.
- Hutchison, W., Babiak, R.J., Finch, A.A., Marks, M.A.W., Markl, G., Boyce, A.J., Stüeken, E.E., Friis, H., Borst, A.M., Horsburgh, N.J., 2019. Sulphur isotopes of alkaline magmas unlock long-term records of crustal recycling on Earth. *Nat. Commun.* 10. <https://doi.org/10.1038/s41467-019-12218-1>.
- Ionov, D.A., Hofmann, A.W., 1995. Nb-Ta-rich mantle amphiboles and micas: implications for subduction-related metasomatic trace element fractionations. *Earth Planet. Sci. Lett.* 131, 341–356. [https://doi.org/10.1016/0012-821X\(95\)00037-D](https://doi.org/10.1016/0012-821X(95)00037-D).
- Ionov, D.A., Griffin, W.L., Reilly, S.Y.O., 1997. Volatile-Bearing Minerals and Lithophile Trace Elements in the Upper Mantle, p. 61.
- Kay, R.W., Kay, S.M., 1993. Delamination and delamination magmatism. *Tectonophysics* 219, 177–189.
- Kelemen, P.B., Manning, C.E., 2015. Reevaluating carbon fluxes in subduction zones, what goes down, mostly comes up. *Proc. Natl. Acad. Sci. U. S. A.* 112, E3997–E4006. <https://doi.org/10.1073/pnas.1507889112>.
- Kelley, D.S., Früh-Green, G.L., 1999. Abiogenic methane in deep-seated mid-ocean ridge environments: insights from stable isotope analyses. *J. Geophys. Res. Solid Earth* 104, 10439–10460. <https://doi.org/10.1029/1999jb900058>.
- Kendrick, M.A., Scambelluri, M., Honda, M., Phillips, D., 2011. High abundances of noble gas and chlorine delivered to the mantle by serpentinite subduction. *Nat. Geosci.* 4, 807–812. <https://doi.org/10.1038/ngeo1270>.
- Kendrick, M.A., Hémond, C., Kamenetsky, V.S., Danyushevsky, L., Devey, C.W., Rodemann, T., Jackson, M.G., Perfit, M.R., 2017. Seawater cycled throughout Earth's mantle in partially serpentinized lithosphere. *Nat. Geosci.* 10, 222–228. <https://doi.org/10.1038/ngeo2902>.
- Keppler, H., Wiedenbeck, M., Shcheka, S.S., 2003. Carbon Solubility in Olivine and the Mode of Carbon Storage in the Earth's Mantle, 424, pp. 414–416. <https://doi.org/10.1038/nature01775.1>.
- Kessel, R., Schmidt, M.W., Ulmer, P., Pettko, T., 2005. Trace element signature of subduction-zone fluids, melts and supercritical liquids at 120–180 km depth. *Nature* 437, 724–727. <https://doi.org/10.1038/nature03971>.
- Konrad-Schmolke, M., Halama, R., 2014. Combined thermodynamic–geochemical modeling in metamorphic geology: boron as tracer of fluid–rock interaction. *Lithos* 208–209, 393–414. <https://doi.org/10.1016/j.lithos.2014.09.021>.
- Li, Y., Wiedenbeck, M., Shcheka, S., Keppler, H., 2013. Nitrogen solubility in upper mantle minerals. *Earth Planet. Sci. Lett.* 377–378, 311–323. <https://doi.org/10.1016/j.epsl.2013.07.013>.
- Lin, L., Hu, Z., Yang, L., Zhang, W., Liu, Y., Gao, S., Hu, S., 2014. Determination of boron isotope compositions of geological materials by laser ablation MC-ICP-MS using newly designed high sensitivity skimmer and sample cones. *Chem. Geol.* 386, 22–30. <https://doi.org/10.1016/j.chemgeo.2014.08.001>.
- Lloyd, N.S., Sadekov, A.Y., Misra, S., 2018. Application of 1013 ohm Faraday cup current amplifiers for boron isotopic analyses by solution mode and laser ablation multicollector inductively coupled plasma mass spectrometry. *Rapid Commun. Mass Spectrom.* 32, 9–18. <https://doi.org/10.1002/rcm.8009>.
- Lu, M., Hofmann, A.W., Mazzucchelli, M., Rivalenti, G., 1997. The Mafic-Ultramafic Complex Near Finero (Ivrea-Verbanio Zone), II. Geochronology and Isotope Geochemistry, 49.
- Mallik, A., Li, Y., Wiedenbeck, M., 2018. Nitrogen evolution within the Earth's atmosphere – mantle system assessed by recycling in subduction zones. *Earth Planet. Sci. Lett.* 482, 556–566. <https://doi.org/10.1016/j.epsl.2017.11.045>.
- Marschall, H.R., Wanless, V.D., Shimizu, N., Pogge von Strandmann, P.A.E., Elliott, T., Monteleone, B.D., 2017. The Boron and Lithium Isotopic Composition of Mid-Ocean Ridge Basalts and the Mantle, *Geochimica et Cosmochimica Acta*. Elsevier Ltd. <https://doi.org/10.1016/j.gca.2017.03.028>.
- Marty, B., Almayrac, M., Barry, P.H., Bekaert, D.V., Broadley, M.W., Byrne, D.J., Ballentine, C.J., Caracausi, A., 2020. An evaluation of the C / N ratio of the mantle from natural CO₂-rich gas analysis: geochemical and cosmochemical implications. *Earth Planet. Sci. Lett.* 551, 116574. <https://doi.org/10.1016/j.epsl.2020.116574>.
- Mazzucchelli, M., Marchesi, S., Bottazzi, P., Ottolini, L., Vannucci, R., 1992. Il corpo peridotitico di Premosello Chiovenza in Val d'Ossola (Zona Ivrea-Verbanio).
- Mazzucchelli, M., Quick, J.E., Sinigoi, S., Zanetti, A., Giovanardi, T., 2014. Igneous evolutions across the Ivrea crustal section: the Permian Sesia magmatic system and the Triassic Finero intrusion and mantle. *Geol. Field Trips*. <https://doi.org/10.3301/gft.2014.05>.
- McDonough, W.F., Sun, S.-S., 1995. The composition of the Earth. *Chem. Geol.* 120, 223–253.
- Mikhail, S., Sverjensky, D.A., 2014. Nitrogen Speciation in Upper Mantle Fluids and the Origin of Earth's Nitrogen-Rich Atmosphere 4–7. <https://doi.org/10.1038/ngeo2271>.
- Moine, B.N., Grégoire, M., O'Reilly, S.Y., Sheppard, S.M.F., Cottin, J.Y., 2001. High field strength element fractionation in the upper mantle: evidence from amphibole-rich composite mantle xenoliths from the Kerguelen Islands (Indian Ocean). *J. Petrol.* 42, 2145–2167. <https://doi.org/10.1093/petrology/42.11.2145>.
- Morishita, T., Arai, S., Tamura, A., 2003. Petrology of an apatite-rich layer in the Finero phlogopite – peridotite, Italian Western Alps; implications for evolution of a metasomatising agent. *Lithos* 69, 37–49. [https://doi.org/10.1016/S0024-4937\(03\)00046-X](https://doi.org/10.1016/S0024-4937(03)00046-X).
- Morishita, T., Hattori, K.H., Terada, K., Matsumoto, T., Yamamoto, K., Takebe, M., Ishida, Y., Tamura, A., Arai, S., 2008. Geochemistry of apatite-rich layers in the Finero phlogopite-peridotite massif (Italian Western Alps) and ion microprobe dating of apatite. *Chem. Geol.* 251, 99–111. <https://doi.org/10.1016/j.chemgeo.2008.02.018>.
- Mysen, B., 2019. Nitrogen in the Earth: abundance and transport. *Prog. Earth Planet. Sci.* 6 (1), 1–15.
- Ottolini, L., Le Fèvre, B., Vannucci, R., 2004. Direct assessment of mantle boron and lithium contents and distribution by SIMS analyses of peridotite minerals. *Earth Planet. Sci. Lett.* 228, 19–36. <https://doi.org/10.1016/j.epsl.2004.09.027>.
- Peressini, G., Quick, J.E., Sinigoi, S., Hofmann, A.W., Fanning, M., 2007. Duration of a large mafic intrusion and heat transfer in the lower crust: a SHRIMP U-Pb zircon study in the Ivrea-Verbanio Zone (Western Alps, Italy). *J. Petrol.* 48, 1185–1218. <https://doi.org/10.1093/petrology/egm014>.
- Plank, T., Manning, C.E., 2019. Subducting carbon. *Nature* 574, 343–352. <https://doi.org/10.1038/s41586-019-1643-z>.
- Porter, K.A., White, W.M., 2009. Deep mantle subduction flux. *Geochem. Geophys. Geosyst.* 10.
- Prouteau, G., Scaillet, B., Pichavant, M., 2001. Hydrous Silicic melts derived from subducted oceanic crust. *Nature* 410, 197–200.
- Quick, J.E., Sinigoi, S., Adriano, Mayer, 1995. Emplacement of mantle peridotite in the lower continental crust, Ivrea-Verbanio zone, northwest Italy. *Geology* 23 (8), 739–742.

- Raffone, N., Le Fèvre, B., Ottolini, L., Vannucci, R., Zanetti, A., 2006. Light-lithophile element metasomatism of finero peridotite (W ALPS): a secondary-ion mass spectrometry study. *Microchim. Acta* 155, 251–255. <https://doi.org/10.1007/s00604-006-0551-8>.
- Rapp, R.P., Watson, E.B., Miller, C.F., 1991. Partial melting of amphibolite/eclogite and the origin of Archean trondhjemites and tonalites. *Precambrian Res.* 51, 1–25. [https://doi.org/10.1016/0301-9268\(91\)90092-O](https://doi.org/10.1016/0301-9268(91)90092-O).
- Rosenthal, A., Hauri, E.H., Hirschmann, M.M., 2015. Experimental determination of C, F, and H partitioning between mantle minerals and carbonated basalt, CO₂/Ba and CO₂/Nb systematics of partial melting, and the CO₂ contents of basaltic source regions. *Earth Planet. Sci. Lett.* 412, 77–87. <https://doi.org/10.1016/j.epsl.2014.11.044>.
- Rosner, M., Erzinger, J., Franz, G., Trumbull, R.B., 2003. Slab-derived boron isotope signatures in arc volcanic rocks from the Central Andes and evidence for boron isotope fractionation during progressive slab dehydration. *Geochim. Geophys. Geosyst.* 4 <https://doi.org/10.1029/2002gc000438> n/a-n/a.
- Rutter, E., Brodie, K., James, T., Burlini, L., 2007. Large-scale folding in the upper part of the Ivrea-Verbano zone, NW Italy. *J. Struct. Geol.* 29, 1–17. <https://doi.org/10.1016/j.jsg.2006.08.013>.
- Ryan, J.G., Langmuir, C.H., 1987. The systematics of lithium abundance in young volcanic rocks. *Geochim. Cosmochim. Acta* 51, 1727–1741.
- Ryan, J.G., Langmuir, C.H., 1993. The systematics of boron abundances in young volcanic rocks. *Geochim. Cosmochim. Acta* 57, 1489–1498.
- Ryan, J.G., Leeman, W.P., Morris, J.D., Langmuir, C.H., 1996. The boron systematics of intraplate lavas: implications for crust and mantle evolution. *Geochim. Cosmochim. Acta* 60, 415–422. [https://doi.org/10.1016/0016-7037\(95\)00402-5](https://doi.org/10.1016/0016-7037(95)00402-5).
- Salter, V.J.M., Stracke, A., 2004. Composition of the depleted mantle. *Geochim. Geophys. Geosyst.* 5.
- Sapienza, G.T., Scambelluri, M., Braga, R., 2009. Dolomite-bearing orogenic garnet peridotites witness fluid-mediated carbon recycling in a mantle wedge (Ulten Zone, Eastern Alps, Italy). *Contrib. Mineral. Petrol.* 158, 401–420. <https://doi.org/10.1007/s00410-009-0389-2>.
- Scambelluri, M., Hermann, J., Morten, L., Rampone, E., 2006. Melt- versus fluid-induced metasomatism in spinel to garnet wedge peridotites (Ulten Zone, Eastern Italian Alps): clues from trace element and Li abundances. *Contrib. Mineral. Petrol.* 151, 372–394. <https://doi.org/10.1007/s00410-006-0064-9>.
- Scambelluri, M., Bebout, G.E., Belmonte, D., Gilio, M., Campomenosi, N., Collins, N., Crispini, L., 2016. Carbonation of subduction-zone serpentinite (high-pressure ophiocarbonate; Ligurian Western Alps) and implications for the deep carbon cycling. *Earth Planet. Sci. Lett.* 441, 155–166. <https://doi.org/10.1016/j.epsl.2016.02.034>.
- Scheele, N., Hoefs, J., 1992. Carbon isotope fractionation between calcite, graphite and CO₂: an experimental study. *Contrib. Mineral. Petrol.* 112, 35–45.
- Schmid, S.M., 1993. Ivrea zone and adjacent Southern Alpine basement. In: *Pre-Mesozoic Geology in the Alps*. https://doi.org/10.1007/978-3-642-84640-3_33.
- Schwarzenbach, E.M., Caddick, M.J., Petroff, M., Gill, B.C., Cooperdock, E.H.G., Barnes, J.D., 2018. Sulphur and carbon cycling in the subduction zone mélange. *Sci. Rep.* 8, 1–11. <https://doi.org/10.1038/s41598-018-33610-9>.
- Shcheka, S.S., Wiedenbeck, M., Frost, D.J., Keppler, H., 2006. Carbon solubility in mantle minerals. *Earth Planet. Sci. Lett.* 245, 730–742. <https://doi.org/10.1016/j.epsl.2006.03.036>.
- Stixrude, L., Lithgow-Bertelloni, C., 2007. Influence of phase transformations on lateral heterogeneity and dynamics in Earth's mantle. *Earth Planet. Sci. Lett.* 263, 45–55. <https://doi.org/10.1016/j.epsl.2007.08.027>.
- Tiepolo, M., Oberti, R., Zanetti, A., Vannucci, R., Foley, S.F., 2007. Trace-element partitioning between amphibole and silicate melt. *Rev. Mineral. Geochem.* 67, 417–452. <https://doi.org/10.2138/rmg.2007.67.11>.
- Tomanikova, L., Savov, I.P., Harvey, J., de Hoog, J.C.M., Churikova, T.G., Gordeychik, B., Yagodinski, G.M., 2019. A Limited Role for Metasomatized Subarc Mantle in the Generation of Boron Isotope Signatures of Arc Volcanic Rocks, 47, pp. 1–5. <https://doi.org/10.1130/G46092.1/4678004/g46092.pdf>.
- Tommasi, A., Langone, A., Padrón-Navarta, J.A., Zanetti, A., Vauchez, A., 2017. Hydrous melts weaken the mantle, crystallization of pargasite and phlogopite does not: insights from a petrostructural study of the Finero peridotites, southern Alps. *Earth Planet. Sci. Lett.* 477, 59–72. <https://doi.org/10.1016/j.epsl.2017.08.015>.
- Tonarini, S., Leeman, W.P., Leat, P.T., 2011. Subduction erosion of forearc mantle wedge implicated in the genesis of the South Sandwich Island (SSI) arc: evidence from boron isotope systematics. *Earth Planet. Sci. Lett.* 301, 275–284. <https://doi.org/10.1016/j.epsl.2010.11.008>.
- Van Keken, P.E., Kiefer, B., Peacock, S.M., 2002. High-resolution models of subduction zones: implications for mineral dehydration reactions and the transport of water into the deep mantle. *Geochim. Geophys. Geosyst.* 3 <https://doi.org/10.1029/2001gc000256>.
- Vannucci, R., Piccardo, G.B., Rivalenti, G., Zanetti, A., Rampone, E., Ottolini, L., Oberti, R., Mazzucchelli, M., Bottazzi, P., 1995. Origin of LREE-depleted amphiboles in the subcontinental mantle. *Geochim. Cosmochim. Acta* 59, 1763–1771. [https://doi.org/10.1016/0016-7037\(95\)00080-J](https://doi.org/10.1016/0016-7037(95)00080-J).
- Vitale Brovarone, A., Martinez, I., Elmaleh, A., Compagnoni, R., Chaduteau, C., Ferraris, C., Esteve, I., 2017. Massive production of abiogenic methane during subduction evidenced in metamorphosed ophiocarbonates from the Italian Alps. *Nat. Commun.* 8, 1–13. <https://doi.org/10.1038/ncomms14134>.
- Wallace, P.J., Plank, T., Edmonds, M., Hauri, E.H., 2015. Chapter 7 – volatiles in magmas. In: *The Encyclopedia of Volcanoes*, Second ed. Elsevier Inc. <https://doi.org/10.1016/B978-0-12-385938-9.00007-9>.
- Watenphul, A., Wunder, B., Wirth, R., Heinrich, W., 2010. Ammonium-bearing clinopyroxene: a potential nitrogen reservoir in the Earth's mantle. *Chem. Geol.* 270, 240–248. <https://doi.org/10.1016/j.chemgeo.2009.12.003>.
- Wolff, R., Dunkl, I., Kiesselbach, G., Wemmer, K., Siegesmund, S., 2012. Thermochronological constraints on the multiphase exhumation history of the Ivrea-Verbano Zone of the Southern Alps. *Tectonophysics* 579, 104–117. <https://doi.org/10.1016/j.tecto.2012.03.019>.
- Zaccarini, F., Stumpfl, E.F., Garuti, G., 2004. Zirconolite and Zr-Th-U minerals in chromitites of the Finero complex, Western Alps, Italy: evidence for carbonatite-type metasomatism in a subcontinental mantle plume. *Can. Mineral.* 42, 1825–1845. <https://doi.org/10.2113/gscanmin.42.6.1825>.
- Zanetti, A., Mazzucchelli, M., Rivalenti, G., Vannucci, R., 1999. The Finero phlogopite-peridotite massif: an example of subduction-related metasomatism. *Contrib. Mineral. Petrol.* 134, 107–122. <https://doi.org/10.1007/s004100050472>.
- Zanetti, A., Giovanardi, T., Langone, A., Tiepolo, M., Wu, F.Y., Dallai, L., Mazzucchelli, M., 2016. Origin and age of zircon-bearing chromitite layers from the Finero phlogopite peridotite (Ivrea-Verbano Zone, Western Alps) and geodynamic consequences. *Lithos* 262, 58–74. <https://doi.org/10.1016/j.lithos.2016.06.015>.
- Zerkle, A.L., Mikhail, S., 2017. The geobiological nitrogen cycle: from microbes to the mantle. *Geobiology* 15, 343–352. <https://doi.org/10.1111/gbi.12228>.
- Zhang, M., Hu, P., Niu, Y., Su, S., 2007. Chemical and stable isotopic constraints on the nature and origin of volatiles in the sub-continental lithospheric mantle beneath eastern China. *Lithos* 96, 55–66. <https://doi.org/10.1016/j.lithos.2006.10.006>.